The human-restricted oncoprotein POU5F1B enhances cell invasiveness through plasma membrane remodeling

Sandra Offner[1], Laurence Abrami[1], Elisa Burri[2], Adrien Mery[3], Barney Drake[3], Jialin Shi[3,4,5], Eduard M Unterauer[6,7], Julien Duc[8], Evarist Planet[1,8], Ralf Jungmann[6,7], Alexandre Reymond[9], Georg Fantner[3], Mahmut Selman Sakar[3], Bernhard Wehrle-Haller[2], F. Gisou van der Goot[1], Didier Trono[1], Laia Simó-Riudalbas[10*]

[1]School of Life Sciences, École Polytechnique Fédérale de Lausanne, Lausanne, Switzerland.
[2]Department of Cell Physiology and Metabolism, University of Geneva, Centre Médical Universitaire, Geneva 4, Switzerland.
[3]School of Engineering, École Polytechnique Fédérale de Lausanne, Lausanne, Switzerland.
[4]State Key Laboratory of Robotics, Shenyang Institute of Automation, Chinese Academy of Sciences, Shenyang 110016, China
[5]Institutes for Robotics and Intelligent Manufacturing, Chinese Academy of Sciences, Shenyang 110169, China
[6]Max Planck Institute of Biochemistry, Planegg, Germany.
[7]Faculty of Physics and Center for NanoScience, Ludwig Maximilian University, Munich, Germany.
[8]Nexco Analytics, Epalinges, Switzerland
[9]Center for Integrative Genomics, Genopode Building, University of Lausanne, Lausanne, Switzerland.
[10]Department of Medicine, Faculty of Medicine, University of Geneva, Centre Médical Universitaire, Geneva 4, Switzerland.

*: Corresponding author: laia.simoriudalbas@unige.ch

Declaration of interests: pending patent application -POU5F1B inhibitors-. Inventors: Laia Simó-Riudalbas, Didier Trono, Gisou van der Goot, Laurence Abrami, Sandra Offner.

Abstract

Evolution confers new species with distinctive biological features that can translate in either purely mechanistic speciation or novel phenotypes. Retrotransposition in the last Hominidae common ancestor of the pluripotency regulator *POU5F1/OCT4* led to human POU5F1B, which promotes gastrointestinal cancer growth and metastasis through unknown mechanisms. Here, we show that POU5F1B fosters cell invasiveness by inducing plasma membrane remodeling. This ability exquisitely depends on a series of post-translational modifications. Ubiquitination of two lysine residues found exclusively in human POU5F1B results in its cytoplasmic retention, contrasting with the nuclear POU5F1. ZDHHC17-mediated S-acylation then triggers POU5F1B association with membrane nanodomains enriched in cell adhesion and signaling molecules. This is accompanied by the cell surface clustering and accelerated turnover of focal adhesion proteins, with enhanced cell invasiveness. Finally, screening for inducers of POU5F1B degradation, we found its stability to depend critically on Rho-associated protein kinases, revealing potential avenues for the treatment of POU5F1B-expressing tumors.

Introduction

Gene duplication is a prominent mechanism of emergence of new gene functions[1]. Transposable elements (TEs) contribute to this process through the generation of mRNA-derived gene duplicates, known as retrogenes. This usually occurs when the reverse transcription machinery of a TE, typically a LINE-1 retrotransposon, captures a cellular mRNA to yield a DNA copy that is then integrated elsewhere in the genome. Long collectively dismissed as non-functional “processed pseudogenes”, retrocopies are increasingly recognized as having contributed a large number of bona fide retrogenes notably in mammals and fruit flies[2–6]. The human genome contains several thousand readily identifiable retrocopies, a few hundreds of which are robustly expressed[7,8]. In most cases, these encode proteins identical to the product of the parental gene, albeit along distinct expression patterns since retrocopies are generally devoid of the source gene regulatory sequences. In a few cases, though, retrogenes undergo neofunctionalization. A typical example is the accumulation in elephant of 19 retrocopies of the tumor-suppressor gene *TP53*, some of which encode gain-of-function proteins responsible for enhanced apoptotic response to DNA damage[9–11]. Both the increased levels of TP53 and the presence of these super-protective variants likely contribute to the rarity of cancer in this species.

The gene encoding OCT4 (octamer-binding protein 4), the well characterized homeodomain transcription factor of the POU (Pit-Oct-Unc) family involved in the self-renewal of embryonic stem cells and in early embryonic development, underwent a series of retroposition events in primates. This resulted in the presence of 6 *POU5F1/OCT4* retrocopies in the human genome, in addition to the parental gene. The youngest, *POU5F1B*, emerged in the last common ancestor of great apes, some 12 million years ago, and is located on chromosome 8q24, proximal to the *MYC* locus. It is transcribed by activation of upstream transposable element-embedded regulatory sequences in several human solid tumors including colon, stomach, breast, prostate and uterus[12]. Its expression is a negative prognostic factor in colorectal[12], gastric[13] and hepatocellular[14] malignancies and is associated with advanced histological grades of cervical cancer[15], where the *POU5F1B* locus is a papillomavirus integration hotspot[16]. Supporting its role as a cancer-promoting factor, the POU5F1B protein stimulates the proliferation of colorectal[12], gastric[13] and hepatocellular[14] carcinoma cells *in vitro* and increases the growth[12,13] and metastatic potential[12] of human gastrointestinal tumor cells in mouse xenotransplantation experiments.

It has been assumed that POU5F1B, like its parental gene OCT4, acts as a stemness-promoting transcription factor. However, we uncovered that despite minor sequence differences, it does not localize to the nucleus but rather to cellular membranes and associates with protein kinases and cytoskeleton-related molecules[12]. We also found that POU5F1B induces intracellular signaling events and the release of trans-acting factors involved in cell growth and cell adhesion[12]. The present study was undertaken to explore further the mechanism of POU5F1B oncogenic action, and notably how it promotes metastases. It reveals that POU5F1B oncogenic function depends on sequential post-translational modifications, some targeting residues unique to the human protein, and on the induction of protein-enriched membrane nanodomains, with augmented cell invasiveness. We also discovered that POU5F1B-induced malignant phenotypes can be reverted by blocking ROCK protein kinases. Thus, POU5F1B is a human-unique oncoprotein that acts by unprecedented mechanisms and can be inhibited through pharmacological approaches.

Results

POU5F1B cytoplasmic localization and function depend on ubiquitination of human-restricted lysine residues

POU5F1/OCT4 and POU5F1B differ by only 15 residues out of 359/360, 5 of which are unique to human POU5F1B, that is, absent from the protein expressed by other great apes (Fig. 1A, Supp. Fig. 1). Yet POU5F1/OCT4 localizes to the nucleus, while POU5F1B accumulates in the cytoplasm[12]. We sought to explain this difference by expressing wild-type and mutated

106 forms of the oncoprotein in SW480 colorectal cancer (CRC) cells. Amongst the 5 human-
107 specific residues of POU5F1B, lysine K135 and K182 stood out as possible targets of
108 ubiquitination, a post-translational modification that can influence the stability, activity and
109 subcellular localization of proteins[17] (Fig. 1A, Supp. Fig. 1). Confirming this hypothesis, we
110 determined that POU5F1B is ubiquitinated and that this modification is largely suppressed
111 when K135 and K182 were changed to glutamic acid and threonine, respectively, as found in
112 POU5F1, or when K182 was substituted by an alanine (Fig. 1B, 1C). Remarkably, the single
113 and double (K135E/K182T) lysine mutants localized to the nucleus (Fig. 1D, 1E). Consistently,
114 inhibiting the ubiquitin activating enzyme with TAK-243[18] triggered the nuclear localization of
115 wild type POU5F1B (Fig. 1D, 1E). We next tested the importance of the cytoplasmic
116 localization of POU5F1B for its ability to promote growth. Replacing either of the two lysine
117 residues specific of POU5F1B by the corresponding amino acid of POU5F1/OCT4 abrogated
118 its growth-promoting action on CRC cells (Fig. 1F).
119
120 **ZDHHC17-mediated acylation is necessary for POU5F1B action on membrane**
121 **nanodomains**
122 We previously reported POU5F1B enrichment in detergent resistant membrane (DRM)
123 fractions of CRC cells[12]. Membrane association of soluble proteins can be induced by covalent
124 linkage of fatty acids, amongst which S-acylation (commonly referred to as S-palmitoylation)
125 plays a particular role in recruitment to DRM subdomains[19,20]. Using the acyl-resin assisted
126 capture (Acylrac) method, whereby S-acylated proteins are trapped on thiol-reactive
127 sepharose beads, we could demonstrate that POU5F1B is S-acylated, and that this
128 modification is reduced by the K135E and K182T mutations (Fig. 2A, 2B). We also found that
129 these amino acid substitutions accordingly impaired POU5F1B association to DRM, assessed
130 using the gradient-based DRM subcellular fractionation as a biochemical readout of
131 cholesterol- and sphingolipid-rich nanodomains[21,22] (Fig. 2C, 2D). Moreover, we observed that
132 wild type POU5F1B expression triggered a significant (>20%) redistribution of transferrin
133 receptor (TFRC), normally a marker of detergent soluble membranes, into DRMs[12] (Fig. 2C,
134 2D). These findings suggest that POU5F1B induces the formation of non-canonical
135 nanodomains in CRC cells. To explore further this phenomenon, we isolated DRMs from
136 SW480 cells overexpressing wild type POU5F1B, its K135E mutant or GFP and analyzed the
137 various fractions of the gradient by Coomassie staining (Supp. Fig. 2A, 2B). Expression of wild
138 type POU5F1B markedly increased the protein content of DRMs, when compared to cells
139 expressing either the K135E mutant or GFP (Supp. Fig. 2A, 2B).
140 S-acylation occurs on cysteines. According to the SwissPalm database
141 (https://swisspalm.org/proteins/Q06416), out of nine such residues present in POU5F1B, only
142 cysteine198 is predicted to be acylated with a high confidence score. We mutated to serine

143 Cys198, as well as Cys185 given its relative proximity (Fig. 2E). We evaluated the dynamics
144 of POU5F1B S-acylation by monitoring the incorporation of radioactive 3H-palmitic acid using
145 immunoprecipitation and autoradiographic analysis. The results confirmed POU5F1B S-
146 acylation (Fig. 2F, 2G), and revealed that this modification was affected more importantly by
147 the C198S than the C185S mutation, yet was dramatically reduced in the C185S/C198S
148 double mutant, suggesting cooperative S-acylation. Correspondingly, this double mutant only
149 marginally associated with DRMs where it failed to induce TFRC recruitment (Fig. 2H, 2I) and
150 protein accumulation (Supp. Fig. 2C, 2D).
151 Protein S-acylation is mediated by protein S-acyltransferases characterized by an aspartate-
152 histidine-histidine-cysteine (ZDHHC) domain. The human genome encodes 23 ZDHHCs, the
153 substrate specificity of which is partly dictated by their subcellular localization[23]. Using siRNAs
154 against each one of these 23 enzymes alone or in combinations, we identified ZDHHC17 as
155 responsible for POU5F1B S-acylation (Fig. 2J, 2K; Supp. Fig. 2E). We next tested whether
156 zDHHC17-mediated acylation affects the membrane association of POU5F1B. We found the
157 DRM-association of POU5F1B to be drastically reduced upon zDHHC17 silencing, which also
158 prevented TFRC redistribution (Fig. 2L, 2M) and protein accumulation (Supp. Fig. 2F, 2G) in
159 DRMs of POU5F1B-expressing cells. In contrast, depleting the acyltransferase had no effect
160 on DRMs in control cells (Supp. Fig. 2F, 2G.
161 Altogether, these observations indicated that POU5F1B associates with cholesterol- and
162 sphingolipid-enriched detergent-resistant nanodomains of the plasma membrane through
163 ZDHHC17-mediated S-acylation, and that it increases their protein recruiting capacity even
164 extending it to proteins such as the transferrin receptor, normally excluded from these
165 domains.
166
167 **POU5F1B triggers the redistribution of cell adhesion proteins and changes in cell**
168 **morphology**
169 The POU5F1B-induced modifications of cell membranes suggested that it might also endow
170 the cell surface with special topographical features. To test this hypothesis, we applied
171 scanning ion conductance microscopy (SICM)[24] (Fig. 3A) to measure cell height and
172 roughness in living GFP-, POU5F1B-, and K135E-POU5F1B-expressing SW480 cells (Fig.
173 3B). The results indicated that wild type POU5F1B-expressing cells were taller than the GFP
174 control and had a rougher surface over the cell body (Fig 3C, 3D) and borders (Fig. 3E) than
175 the two other cell types tested. Images further revealed the presence of membrane protrusions
176 projected upward in the z axis in POU5F1B-expressing cells (Fig. 3B), consistent with our
177 previous finding that levels of ruffle-localized proteins such as SLC9A3R1, CD2AP, RDK and
178 EZR are increased in POU5F1B-expressing cells[12].

179 We next tested whether the physical transformation of the cell surface correlated with a
180 change in its protein content. For this we performed surface biotinylation coupled to
181 precipitation with streptavidin beads on control and dox-inducibly POU5F1B-depleted LS1034
182 CRC cells, which express this protein at baseline and were modified by lentivector-mediated
183 drug-controllable RNA interference. Based on stringent filtering criteria (fold-change in the
184 same direction with two different shRNAs; high intensity candidates –over quantile 25%-; and
185 p value<0.05), we found 142 proteins enriched and 145 depleted in the surface-associated
186 proteome of control compared with POU5F1B-depleted LS1034 cells (Fig. 3F). In their
187 overwhelming majority (274/287), these proteins displayed no difference in total levels,
188 indicating that POU5F1B was acting on their intracellular distribution, not on their expression
189 level (Supp. Fig. 3A). Subjecting the subset of enriched proteins to functional enrichment
190 analysis with the Kyoto Encyclopedia of Genes and Genomes (KEGG) using DAVID
191 knowledgebase v2024q2[25,26] pointed to extracellular matrix (ECM)-receptor interaction
192 molecules as enriched features, notably ITGB1, ITGA1, ITGA2, ITGA9, and ITGAV, which are
193 integrins involved in cell adhesion (Fig. 3G). By contrast, cytoskeletal motor proteins important
194 for vesicle trafficking[27], including dynein, dynactin and myosin, stood out as factors
195 redistributed away from the surface of POU5F1B-expressing cells (Fig. 3G).
196 To investigate proteins enriched in POU5F1B-associated membrane nanodomains, we
197 subjected detergent-treated protein extracts from POU5F1B-knockdown and control LS1034
198 cells to gradient fractionation followed by Coomassie staining (Fig. 3H, 3I) and mass
199 spectrometry analysis (Fig. 3J). Both Coomasie staining and hierarchical clustering of mass
200 spectrometry spectral counts from detergent insoluble F2 and soluble F4-5-6 fractions
201 revealed that the presence of POU5F1B is associated with a higher protein content in DRM
202 fractions (Fig. 3H, 3I, 3J), consistent with the observations made in POU5F1B-overexpressing
203 SW480 cells (Supp. Fig. 2A). Proteins enriched in DRMs of POU5F1B^{+} cells included
204 molecules participating in endocytosis (e.g. RAB proteins), adherent junctions and regulation
205 of actin cytoskeleton (Fig. 3K). As expected from the strong connection between these 3
206 cellular functions, some proteins were classified in two or all three of these categories, e.g.
207 the small GTPase associated with cytoskeleton dynamics and cell migration RHOA, the
208 protein kinases involved in actin cytoskeleton organization, stress fiber and focal adhesion
209 (FA) formation ROCK1 and ROCK2, the stimulator of actin-nucleating activity of the Arp2/3
210 complex WASL, and the focal adhesion components ITGB1, ITGB4, FAK and paxillin (PXN).
211 Signaling molecules such as the signal transduction proteins activated by transforming growth
212 factor (TGF)-beta SMAD2 and SMAD4, the serine/threonine kinase from the MAPK/ERK
213 cascade MAPK1, and the tyrosine kinase FER, which acts downstream of several cell surface
214 receptors, were also enriched in DRMs of POU5F1B+ cells.

215 POU5F1B-triggered protein redistribution was concomitant to a drop in motor proteins
216 association with the cell surface (Fig. 3G) and a DRM enrichment of factors involved in
217 endocytosis, such as the early endosome marker EEA1 and the recycling endosome protein
218 RAB11B (Fig. 3K). This was confirmed by immunofluorescence analysis against early (EEA1),
219 recycling (RAB11B) and late (LBPA, LAMP1) endosomes: while late endosomes/lysosomes
220 were unaffected by the expression of POU5F1B, early and recycling endosomes were more
221 abundant (Supp. Fig. 3B, 3C). Intriguingly, early endosomes were smaller in POU5F1B
222 expressing cells, while recycling endosomes were larger. Regardless the increase in the early-
223 recycling endosomal pathway suggests an accelerated turnover of cell surface components.
224 Taken together, these data indicate that, in colorectal cancer cells, POU5F1B induces
225 changes in the cell surface proteome with alterations of its 2D distribution and of the plasma
226 membrane architecture, as well as modifications in the endosomal recycling pathway.
227
228 **POU5F1B promotes the nano-clustering, surface redistribution and increased turnover**
229 **of focal adhesion proteins**
230 Integrins, which are major components of FAs, were amongst the most surface-enriched
231 DRM-associated proteins in POU5F1B expressing cells (Fig. 3G, 3K). Western blot analysis
232 of total and active form of ITGB1 in the LS1034 knockdown and SW480 overexpression
233 systems confirmed its enrichment in DRMs of POU5F1B-expressing cells (Supp. Fig. 4A, 4B).
234 One of the primary intracellular downstream signalling mediators of integrins is the focal
235 adhesion kinase FAK, which was also highly enriched in DRMs of POU5F1B-expressing cells
236 (Fig. 3K). We examined the cell surface distribution of FA sites by labelling for p-Y^{397}FAK, the
237 form of FAK that becomes phosphorylated and activated upon integrin clustering[28]. To reach
238 high <20 nm spatial resolution, we used the localization-based super-resolution approach
239 DNA-PAINT, which achieves fluorescence separation by the transient interaction of short DNA
240 oligos (Fig. 4A). Quantitative analysis of 75 x 75μm2 fields of view revealed a higher
241 percentage of p-Y^{397}FAK positive sites in POU5F1B-overexpressing than GFP control SW480
242 cells (Fig. 4B), with increased area and number of these sites (Fig. 4C). To characterize further
243 the difference in molecular arrangements of focal adhesion sites, we performed high resolution
244 DNA-PAINT experiments with a localization precision of ~3.5 nm. Using DBSCAN cluster
245 analysis we segmented p-Y^{397}FAK nanoclusters within a detection range of 20nm radius in
246 the adhesion sites (Fig. 4D). We detected a higher number of positive nanoclusters (Fig. 4E)
247 and higher density of molecules within each nanocluster (Fig. 4F) in POU5F1B-expressing
248 compared to control cells.
249 Confocal microscopy images revealed a sharp peripheral ring-like arrangement of p-Y^{397}FAK-
250 positive foci in wild-type, POU5F1B-expressing LS1034 cell colonies, contrasting with a more
251 diffuse pattern in their knockdown counterparts (Supp. Fig. 4C, 4D). We confirmed these

252 results by using total internal reflection fluorescence (TIRF) microscopy, which allows the
253 selective visualization of cellular structures very close to the glass coverslip. We analysed the
254 distribution of talin 1 (Fig. 4G), an integrin adaptor protein shown to activate and to cluster
255 integrins[29], and paxillin (Fig. 4H), which together with FAK is recruited to nascent adhesions
256 at the cell periphery[30]. Measuring the distance of these adhesion structures from the cell
257 periphery to the cell center revealed that POU5F1B-expressing SW480 cells had a more
258 peripheral distribution of talin 1 (Fig. 4I) and paxillin (Fig. 4J) compared with SW480 LacZ
259 control cells, where adhesions were more evenly distributed throughout the cell (Fig. 4I, 4J).
260 This peripheral localization of FA components in POU5F1B-expressing cells coincided with
261 the accumulation of actin filaments close to the cell edges, compared to control cells where
262 they were more diffusely spread (Fig. 4K).
263 Cell movement depends on the assembly and disassembly (turnover) of FAs, which can be
264 used by cancer cells to enhance metastatic dissemination[31]. We previously demonstrated
265 through mouse xenotransplantation experiments that POU5F1B stimulates the formation of
266 metastases by human colorectal cancer cells[12]. We hypothesized that the increased number,
267 size and density of FAs (Fig. 4B-F) and their peripheral redistribution (Fig. 4G-J) in POU5F1B-
268 expressing cells might be accompanied by a faster turnover of their components, which could
269 facilitate cell mobility. To analyse the stability of adhesion structures, we quantified the
270 dissociation rate of Talin1 from FAs via photoactivation experiments[32]. Talin1 was C-terminally
271 tagged with photoactivable GFP, and co-expressed with mCherry-tagged paxillin to identify
272 FAs, in which Talin1 molecules were subsequently photoactivated to study their dissociation
273 rate. The fluorescence loss after photoactivation (FLAP) was recorded for 3 minutes and
274 adhesion stability was assessed by the fluorescence decay in the paxillin-labeled FAs. This
275 analysis showed that POU5F1B expression reduced the stability of Talin1, diminishing its half-
276 life in focal adhesions by 2.4-fold compared to that measured in LacZ control SW480 cells
277 (Fig. 4L-M). Similar results were observed when mcherry-Talin1 labelled adhesion sites were
278 studied for the dissociation rate of photoactivable-GFP labelled paxillin (Fig. 4N-O), a protein
279 we found enriched in DRMs of POU5F1B-expressing cells (Fig. 3K).
280 Thus, our data indicate that POU5F1B-expressing cells harbour more numerous and larger
281 Y^{397}FAK positive adhesive units accumulating in the cell periphery and containing more and
282 denser Y^{397}FAK nanoclusters. In addition, these adhesion structures display a more dynamic
283 exchange of integrin adapter proteins, suggesting an increased ability to turn over adhesion
284 structures towards enhanced cell mobility.
285
286 **POU5F1B drives spontaneous cell invasion in 3D**
287 Cell migration is associated with FA and integrin turnover. The accelerated turnover of FAs
288 observed in POU5F1B expressing cells, led us to evaluate cancer cell invasion using an *in*

289 *vitro* three-dimensional (3D) assay. SW480 cell spheroids were embedded in a collagen-I gel
290 and imaged by confocal microscopy 5 days after seeding (Fig. 5A). POU5F1B-overexpressing
291 SW480 cells presented higher invasion capacity than cells expressing the GFP control or the
292 K135E ubiquitination- or C185S-C198S acylation-defective POU5F1B mutants (Fig. 5B, 5C).
293 We next used a 2D culture system that enables to monitor dissociation of individual cancer
294 cells from 3D CRC spheroids (Fig. 5D). Spheroids were plated onto collagen-I coated dishes,
295 as described[34]. Strikingly, WT POU5F1B-expressing SW480 cells displayed earlier first-cell
296 dissociation times than LacZ-expressing control cells (Fig. 5E, 5F). This accelerated
297 dissociation was abolished by the K135E or K182T mutations, indicating that POU5F1B
298 cytoplasmic localization is necessary for this phenotype. Dissociation of individual cancer cells
299 from 3D CRC spheroids has previously been shown to depend on the viscosity of the
300 medium[33]. We thus switched from normal (0.77 cP) to high viscosity (8cP, achieved with 0.6%
301 of methylcellulose) medium, which mimics the viscosity of body fluids in certain pathological
302 situations[35]. Elevated viscosity accelerated the dissociation of individual cancer cells from 3D
303 CRC spheroids (Fig. 5E, 5F), as previously described[34]. Yet, POU5F1B-expressing SW480
304 cells still displayed earlier first-cell dissociation times than LacZ-expressing controls. Thus
305 POU5F1B induces an increase in cell dissemination from 3D tumor spheroids irrespective of
306 mechanical cues. We further observed that the spheroid initiation capacity of POU5F1B-
307 overexpressing SW480 cells, measured after plating of single cells (Fig. 5D), was greater than
308 that of their K135E-, K182T, or LacZ-overexpressing counterparts (Fig. 5G). Altogether these
309 experiments confirm that POU5F1B-expressing cells are more dynamic, consistent with their
310 higher metastatic potential.
311
312 **Loss of ROCK activity abrogates POU5F1B function**
313 POU5F1B is not endowed with enzymatic activity, and thus could be presumed non-
314 druggable. However, approaches aimed at triggering the proteasomal degradation of
315 pathogenic effectors have changed this perspective, as exemplified by the thalidomide-,
316 lenalidomide-, or pomalidomide-induced degradation of IKZF1 and IKZF3[36–39] for the
317 treatment of multiple myeloma[40]. To explore this avenue, we searched for direct and indirect
318 POU5F1B degraders using a recently described gain-of-signal cell-based assay[41]. For this,
319 we established SW480 cell derivatives expressing POU5F1B fused to deoxycytidine kinase
320 (DCK), an enzyme that converts the non-natural nucleoside 2-bromovinyldeoxyuridine (BVdU)
321 into a poison[42], together with green fluorescence protein (GFP) (Fig. 6A). Parental SW480
322 cells or derivatives expressing wild type POU5F1B or unfused DCK served as controls (Supp.
323 Fig. 5A, 5B). We first confirmed that SW480 cells expressing DCK, either in its native form or
324 fused to POU5F1B, were more sensitive to BVdU than unmodified SW480 cells or cells
325 expressing wild-type POU5F1B (Supp. Fig. 5B). We then exposed POU5F1B-DCK cells in

326 duplicate to a library of 5,758 known bioactive compounds, ~25% of them FDA approved, for
327 24 hours before adding 200 µM BVdU to the culture in order to kill all cells but those in which
328 degradation of the POU5F1B-DCK fusion protein had been induced by the pre-treatment (Fig.
329 6B). This first step of our screen singled out 34 compounds with a Z-score greater than the
330 mean of the negative controls plus three standard deviations (Fig. 6C). These were then used
331 to perform a counter-screen with dose response curves in both POU5F1B-DCK- and DCK-
332 expressing SW480 cells. At the outset of this second step, only two drugs were found to protect
333 POU5F1B-DCK- but not DCK-expressing cells from BVdU-induced death: capivasertib (or
334 AZD5363) and OXA-06, which both are Rho kinase (ROCK) inhibitors (Fig. 6D). Importantly,
335 the two compounds exerted negligible cytotoxicity on unmodified SW480 cells (Fig. 6D).
336 We validated these results by performing pulse-chase experiments with ^{35}SCys/Met in SW480
337 cells. Our results revealed that the half-life of POU5F1B was 60 min in untreated SW480 cells
338 and increased to 160 min in the presence of the proteasome inhibitor MG132 (Fig. 6E),
339 indicating that it is degraded by the proteasome. In sharp contrast, the half-life of POU5F1B
340 dropped to 30 min when cells were treated with capivasertib, OXA-06 or Y-27632, another
341 ROCK inhibitor, yet was restored to 160 min in the combined presence of OXA-06 and MG132
342 (Fig. 6E). This result indicates that ROCK inhibition triggers POU5F1B proteasomal
343 degradation, and in reverse that ROCK stabilizes POU5F1B. The half-life of POU5F1B was
344 similarly reduced upon dox-inducible ROCK1 knockdown (Fig. 6F, Supp. Fig. 5C).
345 Furthermore, upon 24 hours of either OXA-06 treatment (Fig. 6G, 6H) or ROCK1
346 downregulation (Fig. 6I, 6J), the overall protein content of DRMs (fraction 2) decreased in
347 POU5F1B-overexpressing but not control SW480 cells (Fig. 6G, 6H, 6I, 6J). Interestingly, a
348 stronger effect was observed upon ROCK1 than ROCK2 downregulation, indicating that
349 POU5F1B is more dependent on ROCK1 in these cells (Fig. 6I, 6J). Consistently,
350 downregulation of ROCK1 lowered the amount of POU5F1B associated with DRMs (Supp.
351 Fig. 5D). Noteworthy, the remaining amounts of ROCK1 were also no longer found in DRMS
352 in this setting (Supp. Fig. 5D). Finally, ROCK1 downregulation decreased the invasion
353 capacity of POU5F1B-overexpressing SW480 cells in the 3D spheroid invasion assay,
354 whereas it had no effect on control cells (Fig. 6K, 6L).
355

356 ## Discussion

357 Our work demonstrates that the product of the human ortholog of the hominoid-restricted
358 *POU5F1B* gene is endowed with unique properties dependent on sequential ubiquitination
359 and S-acylation. The first of these post-translational modifications targets residues specific to
360 the human protein, meaning that *POU5F1B* represents a human-unique cancer-promoting
361 gene, to our knowledge the first described to date. While another human-specific retrogene,

362 *NANOGP8*, has also been found overexpressed in some cancers, its product is similar in
363 sequence and function to that of its parental *NANOG* gene, which encodes a well
364 characterized stemness-promoting transcription factor[43]. As well, although the onco-
365 exaptation of human-restricted TE integrants could theoretically result in the making of
366 oncoproteins with unique properties, in examples investigated so far the function of the product
367 made from these TE-driven aberrant transcripts was found to be similar to that of their native
368 counterparts, for example the AluJb-LIN28B fusion protein that carries the same function as
369 LIN28B despite a 22 residue-long N-terminal extension[44].
370 Our biochemical and functional studies demonstrate that POU5F1B exerts its pro-oncogenic
371 action through an unprecedented mechanism: the formation of non-canonical protein-enriched
372 membrane nanodomains. Membrane nanodomains are known to play important role in signal
373 transduction through their capacity to act as protein concentrating platforms[45]. Malignant cells
374 exploit these platforms to initiate oncogenic signaling and promote tumor progression[46].
375 Although many studies have focused on the consequences of nanodomain formation in cancer
376 biology[46], little is known about the intracellular mechanisms fostering their assembly in this
377 context. Membrane nanodomains are known to be enhanced by extracellular cues such as
378 cell-to-cell contacts, as in the setting of the immune synapse[47], or by ECM-to-cell contacts, as
379 when migrating cells concentrate adhesion proteins in response to increased ECM stiffness[48].
380 The ECM component agrin had been found to foster the clustering of membrane nanodomains
381 in both immune and nervous synapses[49]. Here we identify POU5F1B as stimulating the
382 remodeling of membrane nanodomains from inside the cells, profoundly remodeling their
383 protein content. We discovered several signaling molecules (e.g. SMAD2, SMAD4, MAPK1,
384 FER) to be enriched in DRMs of POU5F1B positive cells, and we previously reported that
385 POU5F1B co-immunoprecipitates with a number of signaling proteins (e.g. ERBB2, MST1R,
386 PRKCA)[12]. DRMs of POU5F1B-expressing cells were also enriched with FA-building proteins,
387 which organized in high-density FA structures that displayed increased rates of turnover and
388 colocalized with a peripheral organization of actin filaments. We also observed the
389 accumulation of RhoA, ROCK1 and ROCK2 in these altered membrane nanodomains and
390 discovered that POU5F1B-triggered phenotypes depend on the activity of ROCK, the
391 blockade or depletion of which destabilized the oncoprotein. It has been previously shown that
392 activated RhoA increases myosin-dependent contraction of the actin cytoskeleton[50], leading
393 to intracellular tension and increased turnover of integrins in FAs[51], a prerequisite for cell
394 migration. This could partially explain why POU5F1B-expressing cells are capable of migrating
395 faster out of a spheroid even in the absence of an external physical stimulation (e.g. increase
396 of medium viscosity). Although we observed that POU5F1B positive cells transform
397 membrane nanodomains into denser signaling and adhesion platforms, we do not know yet

398 whether signaling and adhesion molecules are found within the same or distinct sets of
399 nanodomains.
400 The continuous endocytosis and recycling to the plasma membrane of focal adhesions
401 building blocks is an essential component of cell movement[52], and cholesterol-sphingolipid
402 rich membrane nanodomains are implicated in endocytosis[53], sorting and recycling[54–56]
403 processes. Accordingly, we describe here that POU5F1B-expressing cells have membrane
404 nanodomains enriched in endocytic proteins, and display an enhanced vesicular endocytic-
405 recycling pathway as well as a higher turnover of focal-adhesion related molecules. We
406 previously observed these cells present increased levels of caveolin-1 and other components
407 of caveolae[12], which are the invaginated form of plasma membrane nanodomains[57] that
408 associate with the activation of the contractile actin cytoskeleton and favor cell migration[58]. It
409 suggests that POU5F1B-induced alterations in endocytosis and recycling might proceed
410 through caveolae.
411 The actin-myosin cytoskeleton and its regulatory axis Rho GTPase-ROCK proteins are used
412 by cancer cells to migrate and metastasize[59,60]. ROCK proteins regulate cell contractility, actin
413 cytoskeleton organization and FA formation, which we found to be enhanced by POU5F1B.
414 Future studies will address whether POU5F1B is a direct target of ROCK or whether it is
415 stabilized by interacting with a ROCK-phosphorylated partner. Our pharmacological and
416 genetic data concur to demonstrate that ROCK activity is essential to the stability hence the
417 function of POU5F1B. Indeed, blocking or depleting the kinase triggers POU5F1B
418 proteasomal degradation, with *ROCK1* knockdown abrogating the increased cell invasiveness
419 induced by the retrogene product in a 3D spheroid assay. While ROCK inhibitors have so far
420 been seldom used to treat cancer[61–63], our data warrant exploring their therapeutic potential
421 under the lens of POU5F1B expression, whether as a biomarker for patient stratification or to
422 guide the selection of specific inhibitors.
423 *POU5F1B* emerged as the result of a retrotransposition event that occurred some 12 to 15
424 million years ago. The physiological roles of its human product and the nature of the pressures
425 that drove its selection during the last 5 to 7 million years, that is, after the human-chimpanzee
426 split, remain to be identified. Irrespectively, as the product of a retrogene expressed in cancer
427 by aberrant activation of upstream TE-embedded regulatory sequences, POU5F1B provides
428 a multifaceted illustration of the prominent role played by transposable elements in conferring
429 an often-underestimated degree of species-specificity to the biology of higher vertebrates.
430
431

Acknowledgements

We thank the members of Alexandre Reymond's and Didier Trono's laboratories for stimulating discussions. We gratefully acknowledge the Proteomics Core Facility (PCF), and the Bioimaging and Optics Platform (BIOP) at EPFL, as well as the Imaging Platform ACCESS and the imaging core facility (CMU) at the University of Geneva for their skilful assistance. We are particularly grateful to David Root (Genetic Perturbation Platform, Broad Institute of Harvard and MIT) for helping us set up the screen for inducers of POU5F1B degradation. This work was supported by grants from the European Research Council (Transpos-X, No. 694658), the Personalized Health and Related Technologies (PHRT-508) program, the Swiss National Science Foundation (310030-152879, 310030B-173337, 310030-18803, 320030-227571, 310030-192613 and 1310030-219201), and the Novartis foundation No. 532316 to D.T., the Swiss Cancer Research Foundation (KFS-4968-02-2020 and KFS-5823-02-2023) to D.T. and L.S.R., the UNIL Tremplin grant to L.S.R., and grants from the Swiss National Science Foundation to B.W.H. (320030-228395) and GVDG. G.E.F. acknowledges the support of the H2020 - UE Framework Programme for Research & Innovation (2014-2020); ERC-2017-CoG; InCell; Project number 773091, and the EPFL Centre for Imaging, grant number 21645. The authors acknowledge the use of BioRender.com for the creation of the graphical abstract and the model depicted in Figure 6M.

451 # Methods

452

453 **Cell culture.** LS1034 and SW480 cell lines were obtained from the American Type Culture
454 Collection (ATCC) and maintained in RPMI 1640 (Gibco) and L15 medium (Sigma)
455 respectively, being supplemented with 10% FCS (Bioconcept 2-01F36-I). For lentiviral vector
456 production, 293T cells were cultured in DMEM supplemented with 10% FBS with 100 IU ml^{-1}
457 penicillin, 100 ug ml^{-1} streptomycin, and 26 µg ml^{-1} glutamine (Corning 30-009-CI) at 37°C in
458 a humidified atmosphere of 5% CO_2. All cells tested negative for mycoplasma.
459 **Overexpression and shRNA vectors.** For the POU5F1B-expressing vector, genomic DNA
460 from DLD1 cells (ATCC® CCL-221™) was PCR amplified with the POU5F1B primers 5'-
461 CACCATGGCGGGACACCTGGCTTCGGATTTC-3', 5'-
462 GTTTGAATGCATGGGAGAGCCCAG-3', cloned into a pENTR TOPO donor vector (Thermo
463 Fisher), that was recombined with the doxycycline-inducible lentiviral destination vector pSin-
464 TRE-3xHA-puro. For the DCK-based positive selection assay, we kindly received from William
465 Kaelin's laboratory the pLX304-gate-DCK-V5-IRES-GFP plasmid, in which we Gateway
466 cloned *POU5F1B*. Short hairpin RNA (shRNA) were designed with the help of the i-Score
467 Designer website, and adapted to the miR-E shRNA structure and cloned into the LT3GEPIR
468 pRRL backbone following Fellmann C et. al. instructions[64]: shRNA3 5'-
469 TGCTGTTGACAGTGAGCG**CACAGGTGATTATGATTTAAAG**TAGTGAAGCCACAGATGT
470 A**CTTTAAATCATAATCACCTGTG**TGCCTACTGCCTCGGA-3'; shRNA5 5'-
471 TGCTGTTGACAGTGAGCG**CACATTCAGTCAACATTTAATG**TAGTGAAGCCACAGATGT
472 A**CATTAAATGTTGACTGAATGTG**TGCCTACTGCCTCGGA-3') with a scrambled shRNA
473 serving as negative control 5'-
474 TGCTGTTGACAGTGAGCG**CAACAAGATGAAGAGCACCAAG**TAGTGAAGCCACAGATG
475 TA**CTTGGTGCTCTTCATCTTGTTG**TGCCTACTGCCTCGGA-3'.
476 **Lentivirus production and stable gene expression.** Lentiviral particles produced as
477 described at http://tronolab.epfl.ch were used to transduce SW480 and LS1034 cells in 6-well
478 plates at multiplicity of infection 1, before selection in 1 µg ml^{-1} puromycin for 7 days.
479 POU5F1B, GFP and lacZ overexpression in SW480 cells was verified, after three days of 500
480 ng ml^{-1} doxycycline activation, by western blot with HRP-conjugated anti-HA antibody (clone
481 3F10 Roche 12013819001, 1:1,000); and *POU5F1B* downregulation upon shRNA
482 transduction in LS1034 was analyzed by quantitative real-time PCR using P3 pair of primers[12].
483 Constitutive expression of POU5F1B-DCK and DCK proteins was verified by western blot with
484 anti-V5 antibody.
485 **Immunofluorescence.** Cell lines were plated on glass coverslips into 24-well plates and
486 cultured for 3 days up to 70% confluence in 500 ng ml^{-1} doxycycline-containing medium.
487 Growth medium was refreshed (1 ml) prior a 15 min fixation with 1 ml 8% paraformaldehyde

488 (PFA) added dropwise, to achieve a final concentration of 4% PFA. Cells were washed three
489 times with PBS, permeabilized with 0.05% saponin PBS for 20 min, and blocked with 1% BSA
490 0.05% saponin PBS for 30 min before incubation with anti-HA (bioLegend, Covance catalog
491 #MMS-101P, 1:1,000) and anti-lamin-B1 (abcam ab16048, 1:1,000) antibodies in 1% BSA
492 0.05% saponin PBS 2 h at room temperature (RT) under agitation. Phospho-FAK Tyr397
493 (Thermofisher 700255, 1:200) antibody was incubated overnight at 4 degrees in blocking
494 solution without saponin. Samples were washed three times with PBS and incubated with
495 Alexa 647-conjugated (A647) anti-mouse antibody (1:1,000) and A568 anti-rabbit antibody
496 (1:1,000) in 1% BSA PBS for 40 min at RT. Three final washes were performed before
497 mounting the slides in Vectashield with DAPI (Vector Laboratories). Images were acquired on
498 a ZEISS LSM 700 confocal microscopy and analyzed with Fiji software.
499 **Immunoprecipiation and western blot.** For immunoprecipitation and western blot, cells were
500 lysed on ice for 30 min with lysis buffer (500 mM Tris–HCl pH 7.4, 2 mM benzamidine, 10 mM
501 NaF, 20 mM EDTA, 0.5% NP40 and a protease inhibitor cocktail (Roche, CH)). Samples were
502 sonicated using a probe sonicator (two times 5 seconds at 30% amplitude). The lysate was
503 then clarified by centrifugation at 4 °C for 5 min at 5000 rpm and incubated overnight on a
504 rotating wheel at 4 °C with 50 µl of HA coupled agarose beads (Sigma 11867423001). The
505 beads were then washed 3× with lysis buffer before adding 4× Sample Buffer including beta-
506 mercaptoethanol. Similar elution volumes and protein quantities for the IPs and the inputs,
507 respectively, were submitted to SDS-PAGE and analyzed by immunoblotting using HRP-
508 conjugated anti-HA (clone 3F10 Roche 12013819001, 1:1,000) and anti-Ubiquitin antibody.
509 ***In vitro* proliferation assays.** Cell proliferation was determined with PrestoBlue™ reagent
510 (A13262, Invitrogen) for 6 days.
511 **Isolation of detergent-resistant membranes (DRMs).** Approximately 1 × 10^7 cells were
512 resuspended in 0.5 ml cold TNE buffer (25 mMTris-HCl, pH 7.5, 150 mM NaCl, 5 mM EDTA,
513 and 1% Triton X-100; Surfact-Amps, ThermoFisher) with a tablet of protease inhibitors
514 (Roche). Membranes were solubilized in a rotating wheel at 4 °C for 30 min. DRMs were
515 isolated using an Optiprep™ gradient [65]: the cell lysate was adjusted to 40% Optiprep™,
516 loaded at the bottom of a TLS.55 Beckman tube, overlaid with 600 µl of 30% Optiprep™ and
517 600 µl of TNE, and centrifuged for 2 h at 55,000 rpm at 4 °C. Six fractions of 400 µl were
518 collected from top to bottom. DRMs were found in fraction 2. Equal volumes from each fraction
519 were analyzed by SDS-PAGE and western blot analysis using HRP-conjugated anti-HA,
520 caveolin1 (Santa Cruz sc-894, 1:500) and transferrin receptor (ThermoFisher 13-6800,
521 1:1,000) antibodies.
522 **Acyl-RAC capture assay**. Protein S-palmitoylation was assessed by the Acyl-RAC assay as
523 previously described[66] with some modifications. Cells or supernatants were lysed in 400 ml
524 buffer (0.5% Triton-X100, 25 mM HEPES, 25 mM NaCl, 1 mM EDTA, pH 7.4,and protease

525 inhibitor cocktail). Cell lysis were incubated 30 min at RT with 10mM TCEP. Then, 200 ml of
526 blocking buffer (100 mMHEPES, 1 mM EDTA, 87.5 mM SDS, and 1.5% [v/v] methyl
527 methanethiosulfonate (MMTS)) was added to the lysates and incubated for 4 h at 40ºC to
528 block free the SH groups with MMTS. Proteins were acetone precipitated and resuspended in
529 buffer (100 mMHEPES, 1 mM EDTA, 35 mM SDS). For treatment with hydroxylamine
530 (NH2OH) and capture by Thiopropyl Sepharose beads, 2 M of hydroxylamine was added
531 together with the beads (previously activated for 15 min with water) to a final concentration of
532 0.5 M of hydroxylamine and 10% (w/v) beads. As a negative control, 2 M Tris was used instead
533 of hydroxylamine. These samples were then incubated overnight at room temperature on a
534 rotating wheel. After washes, the proteins were eluted from the beads by incubation in 40 µl
535 SDS sample buffer with ß-mercaptoethanol for 5 min at 95ºC. Finally, samples were separated
536 by SDS-PAGE and analyzed by Western blot. A fraction of the cell lysate (total cell extract)
537 was saved as the input.
538 **Radiolabeling 3H-palmitic acid incorporation.** To follow S-acylation, lentiviral vector
539 transduced and 96h doxycycline activated cells were incubated 1 hour in L15 medium without
540 serum, followed by 2 hours at 37ºC in L15 without serum with 200 uCi /ml 3 H palmitic acid,
541 washed with cold PBS, and lysed with RIPA buffer prior overnight anti-HA
542 immunoprecipitation. Beads were incubated 5 min at 90ºC in reducing sample buffer prior to
543 SDS-PAGE. Immunoprecipitates were split into two, run on 4-20% gels and analyzed either
544 by autoradiography (3 H-palmitate) after fixation (25% isopropanol, 65% H2O, 10% acetic
545 acid), incubation 30 min in enhancer Amplify NAMP100, and drying; or western blot.
546 **Transfection of siRNA.** SW480 cells were transfected with siRNA (Qiagen, Supplementary
547 Table S1) (15 pmol/ 9.6cm2 plate) using Lipofectamine RNAiMAX transfection reagent. Cells
548 were harvested 72h post transfection and whole cell protein lysates were analyzed by western
549 blot.
550 **Scanning ion conductance microscopy (SICM) imaging, data processing and analysis.**
551 Images from live SW480 cells were taken in L-15 (Leibovitz) medium, at 37°C and saturated
552 humidity. Imaging was performed with bias voltages of 200 to 300mv, 2 to 4nA ion currents
553 and typical pipette tip inner diameters of 100nm. A detailed description of the homebuilt
554 microscope platform has been published here[24]. SICM images were processed using
555 Gwyddion[67]. Image defects with the maximum width of 1 pixel were removed by filling-in the
556 neighboring line. The cells were marked by implementing height thresholding, with the height
557 data of the images leveled by shifting the mean height value of the substrate part to zero. To
558 analyze the roughness and height of the cell, we separated the small structure on the cell
559 membrane surface from the cell topography by using frequency split or two polynomial degree
560 leveling. The cell bodies were masked by shrinking the mask of the cells. The root mean
561 square roughness of a cell body and boarder were calculated from the high frequency image,

562 and cell height was extracted by using the max value of the low frequency image. All SICM
563 topography data were normalized by 13 µm and exported in 16-bit Portable Network Graphics
564 format with gray and customized color bar. We used the open-source 3D rendering tool
565 Blender 3D to generate the three-dimensional images of the cells. The corresponding SICM
566 height data and colored data were imported and used as a height map and projected color on
567 the topography.
568 **Cell surface protein studies.** Surface biotinylation assays were performed as previously
569 described[68]. Briefly, cells were shifted to ice and incubated for 30 min with cold biotinylation
570 solution (0.2 mg/ml sulfo-NHS-SS-biotin (Pierce) diluted in PBS -0.17-mg/mL final
571 concentration-), then quenched three times with cold 100 mM NH4Cl, and lysed in IP buffer.
572 The lysate was immunoprecipitated overnight at 4°C with prewashed streptavidin-coated
573 beads (Sigma S1638), beads were washed with 1 mL 1% SDS, 150 mM NaCl, 1 mM EDTA
574 in 50 mM HEPES pH 7.4 (×3) and 50 mM HEPES pH 8.0 (×2), and proteins were eluted from
575 beads with 50 µL of 50 mM HEPES pH 8.0 containing 50-100 mM TCEP for 1 h. Peptides
576 containing supernatants were digested overnight at 37 ºC in the thermoshaker with 1-2 µL
577 Trypsin (20 µg /100 µL) in 50 mM HEPES pH 8. For LC MS/MS analysis, peptides were
578 resuspended and separated by reversed-phase chromatography on a Dionex Ultimate 3000
579 RSLC nanoUPLC system in-line connected with an Orbitrap Lumos Fusion Mass-
580 Spectrometer. Database search was performed using MaxQuant 1.6.10.43[69] against
581 concatenated database consisting of the UniProt human database (Uniprot release 2019_06,
582 74468 sequences) and common fetal bovine serum protein[70]. Raw spectral counts extracted
583 with MaxQuant were subjected to log2 transformation, and any missing values were imputed
584 using the 'min' function available in the DEP package[71]. Proteins that exhibited fewer than 10
585 log2-transformed total spectral counts across all samples were excluded for further analysis.
586 To identify proteins undergoing significant changes between conditions of interest, a statistical
587 linear model with interactions was applied using the limma R package[72]. Surface-associated
588 proteome candidates were selected when the three experimental replicates showed p
589 value<0.05 (outlier detection test as computed by MaxQuant), high intensity (above quantile
590 25%), and fold changes in the same direction for the two shRNAs.
591 **LC-MS/MS analysis of DRM fractions.** DRM fraction 2 (F2) and equal volume mixes of
592 fractions 4, 5, and 6 (F456) from shRNA-scramble, shRNA3 and shRNA5-transduced LS1034
593 cells were analyzed by Liquid Chromatography with tandem mass spectrometry (LC-MS-MS).
594 Each sample was digested by Filter Aided Sample Preparation (FASP)[73] with minor
595 modifications. Dithiothreitol (DTT) was replaced by Tris (2-carboxyethyl)phosphine (TCEP) as
596 reducing agent and Iodoacetamide by Chloracetamide as alkylating agent. A combined
597 proteolytic digestion was performed using Endoproteinase Lys-C and Trypsin. Peptides were
598 desalted on SDB-RPS StageTips[74] and dried down by vacuum centrifugation. Samples were

599 then fractionated into 12 fractions using an Agilent OFFGEL 3100 system. Resulting fractions
600 were desalted on SDB-RPS StageTips and dried by vacuum centrifugation. Samples were
601 analyzed by LC-MS/MS as described above. Proteins that demonstrated notably different
602 behavior between the 'scramble' and 'sh' conditions in F2 compared to their F456
603 counterparts, and exhibited a foldChange of less than 0.5 log2 in all 'inputs', were selected for
604 further analysis.
605 **DAVID enrichment analysis.** For DRM and surface associated-proteome data sets, we
606 obtained a list of differentially expressed candidates that were selected as detailed above.
607 Resulting candidate lists were subjected to GO and KEGG functional annotation chart using
608 the online bioinformatics resource DAVID[25,26].
609 **High resolution microscopy imaging.**
610 Buffers for super-resolution experiments. The following buffers were used for sample
611 preparation and imaging:
612 • Buffer C+: 1× PBS, 500 mM NaCl and 0.05% Tween-20 (Sigma Aldrich cat: P9416-50ML)
613 • Buffer C: 1× PBS, 500 mM NaCl
614 • Antibody Incubation buffer: 1×PBS, 1 mM EDTA, 0.02% Tween-20, 0.05% NaN3, 2% BSA
615 (Sigma Aldrich cat: A4503-10G), and 0.05 mg/ml sheared salmon sperm DNA (Thermo Fisher
616 cat: 15632011)
617 • Blocking Buffer: 1×PBS, 1 mM EDTA, 0.02% Tween-20, 0.05% NaN3, 2% BSA (Sigma
618 Aldrich cat: A4503-10G), 0.05% saponin and 0.05 mg/ml sheared salmon sperm DNA
619 (Thermo Fisher cat: 15632011)
620 • Imaging solution: Buffer C+ supplemented with oxygen scavenger system (1x Trolox, PCA,
621 PCD)
622 Oxygen scavenger system preparation. 100× Trolox (Sigma Aldrich cat: 238813-5 G): 100 mg
623 Trolox was added to 430 µl 100 % Methanol, 345 µl 1M NaOH, and 3.2 ml H2O. 40× PCA
624 (Sigma Aldrich cat: 37580-25G-F): 154 mg PCA, 10 ml water and NaOH were mixed and pH
625 was adjusted 9.0. 100× PCD (Sigma Aldrich cat: P8279): 9.3 mg PCD, 13.3 ml of buffer (100
626 mM Tris-HCl pH 8, 50 mM KCl, 1 mM EDTA, 50 % Glycerol).
627 Nanobody-DNA conjugation via single cysteine. Rabbit secondary nanobodies were
628 purchased from Nanotag (cat: N2405) with a single ectopic cysteine at the C-terminus for site-
629 specific and quantitative conjugation. The conjugation to DNA-PAINT docking site 7xR4 –
630 ACACACACACACACACACA with a 5' C-3 azide (Metabion) - was performed as previously
631 described (cite: doi.org/10.1039/D0NR00227E). In brief, the buffer was exchanged to 1× PBS
632 + 5 mM EDTA, pH 7.0 using Amicon centrifugal filters (10k MWCO) and free cysteines were
633 reacted with a 20-fold molar excess of bifunctional maleimide-DBCO linker (Sigma Aldrich,
634 cat: 760668) for 2-3 hours on ice. The unreacted linker was removed by buffer exchange to
635 PBS using Amicon centrifugal filters. Azide-functionalized DNA was added with 3-5 molar

636 excess to the DBCO-nanobody and reacted overnight at 4°C. Unconjugated nanobody and
637 free azide-DNA were removed by anion exchange using an ÄKTA Pure liquid chromatography
638 system equipped with a Resource Q 1 ml column. Nanobody-DNA concentration was adjusted
639 to 5 µM (in 1xPBS, 50% glycerol, 0.05% NaN3) and stored at -20°C.
640 Super-resolution microscopy setup. Super-resolution DNA-PAINT imaging was performed on
641 an inverted Eclipse Ti2 microscope (Nikon Instruments) with a Perfect Focus System unit,
642 applying an objective-type TIRF configuration equipped with an oil-immersion objective (Nikon
643 Instruments, Apo SR TIRF×100, NA 1.49, Oil). A 560-nm laser (MPB Communications, 1 W)
644 was used for fluorophore excitation and coupled into the microscope via a Nikon manual TIRF
645 module. The laser beam was passed through a cleanup filter (Chroma Technology,
646 ZET561/10) and further coupled into the microscope objective using a beam splitter (Chroma
647 Technology, ZT561rdc). Fluorescence was spectrally filtered with an emission filter (Chroma
648 Technology, ET600/50m, and ET575lp) and detected on an sCMOS camera (Hamamatsu
649 Fusion BT) without further magnification, resulting in an effective pixel size of 130 nm after
650 2×2 binning. TIR illumination was used for all measurements. The central 1152×1152 pixels
651 (576×576 after binning) of the camera were used as the imaging field of view (FOV). Raw
652 microscopy data was acquired using µManager (Version 2.0.1) (cite: doi:
653 10.14440/jbm.2014.36).
654 DNA-PAINT sample preparation and imaging. SW480 POU5F1B-overexpressing and GFP
655 control cell lines were seeded with approximately 30K cells per cm2 in 8-well ibidi µ-slides
656 (ibidi cat: 8080) with doxycycline supplemented media (500 ng/ml) for 96 h (replenishment
657 with fresh media after 48h). Afterwards cells were fixed with 4% PFA, washed 4 times with
658 PBS and permeabilized with 0.05% saponin in PBS for 15 min. Cells were then washed with
659 PBS three times and blocked with Blocking buffer for 30 min. After 3 times washing with PBS
660 90 nm gold nanoparticles (1:2, Cytodiagnotics cat: G-90-100) were incubated onto the sample
661 for 5 min followed by 3 times washing with PBS. Phospho-FAK (Tyr397) Recombinant Rabbit
662 Monoclonal Antibody (31H5L17) (Thermo Fisher cat:700255) was diluted 1:200 and put onto
663 the sample in antibody incubation buffer overnight. The next morning the sample was washed
664 4 times with PBS and a 1:200 dilution of rabbit secondary nanobody (7xR4) (Nanotag cat:
665 N2405) was introduced to the sample in antibody incubation buffer (concentration of ~50 nM)
666 for ~1 h. Finally, the sample was washed 4 times with PBS, once with buffer C and then
667 incubated with imaging solution. For low resolution, high statistics experiments, the samples
668 were supplemented with 500 pM R4 imager - TGTGTGT-Cy3B - (Metabion) containing
669 imaging solution. The samples were mounted onto the microscope stage and 7.500 75 ms
670 frames were acquired at a laser power of 30 mW (~150 W/cm2). To ensure unbiased detection
671 of highly expressing p-Y397FAK focal adhesion sites, FOV selection was done in brightfield.
672 Three distinct samples per condition were imaged. For high resolution experiments the

673 samples were supplemented with 100 pM R4 imager containing solution and 40.000 100 ms
674 frames were acquired at 30 mW laser power. In order to select only highly expressing p-
675 Y397FAK focal adhesion sites, FOV were prescreened with a high (500 pM) imager
676 concentration and afterwards incubated with 100 pM imager for highest resolution imaging.
677 Single-molecule localization analysis. Raw fluorescence data was reconstructed using the
678 Picasso software package (cite:doi.org/10.1038/nprot.2017.024) (the latest version is
679 available at https://github.com/jungmannlab/picasso). Drift correction was performed using the
680 AIM algorithm (cite: /doi.org/10.1126/sciadv.adm7765) with 90 nm gold nanoparticles
681 (Cytodiagnotics cat: G-90-100) as fiducials for all experiments.
682 p-Y397FAK postprocessing analysis. For the low resolution, high statistics experiments, the
683 75 x 75 µm2 FOVs of POU5F1B-overexpressing and GFP control datasets were segmented
684 for high intensity p-Y397FAK regions. First, gold nanoparticles were removed from localized
685 and drift-corrected DNA-PAINT. The datasets were blurred using a 400 nm 2D bin size and
686 2.5 as gaussian blur in bin size units. The threshold for the masked region was set to 350
687 localizations for the p-Y397FAK regions and to 100 localizations for segmentation of the cell
688 area (in a blurred bin), ensuring comparable segmentation of POU5F1B-overexpressing and
689 GFP control samples. Area and density were calculated using the number of localizations
690 inside the 2D binned masked regions.
691 For the high-resolution datasets, a 350 nm bin size 2D mask with 1.5 gaussian blur was
692 generated for all datasets to mask the p-Y397FAK regions. The threshold was normalized to
693 0.15 times the brightest bin, which were generated using gold nanoparticles. After the masks
694 were generated, gold was removed from the datasets. All localizations inside the masked
695 regions were extracted and DBSCAN using 20 nm as search radius (approximately the label
696 size of antibody and secondary nanobody) with minimal sample size of 40 localizations. With
697 an imager concentration of 100 pM and 40.000 frames the expected number of binding events
698 for R4 (on rate, kon of 27 * 106) (cite: doi.org/10.1038/s41592-020-0869-x) can be calculated.
699 Using kon*cR4 = ξ , with c as concentration and ξ as influx rate, the influx rate of the
700 measurements yields 0.0027 s-1 (cite: doi.org/10.1038/nmeth.3804). Since the total imaging
701 time equals 40.000 times 100 ms, the total number of binding events in that duration is ~10.
702 Assuming a bright time of 0.4 s, a single binding event will result in 4 localizations for a single
703 binding site, resulting in ~40 localizations over the entire measurement. The area, localization
704 numbers and densities for the DBSCAN clusters of POU5F1B-overexpressing and GFP
705 control samples were then extracted on an individual cluster level for all datasets.
706 **Focal adhesion centrality analysis using total internal reflection fluorescence (TIRF)**
707 **microscopy.** LacZ-, and POU5F1B-expressing SW480 cells were transiently transfected with
708 pcDNA3-mCherry-paxillin or pcDNA3-mCherry-talin1 using the JetPrime reagent (Polyplus)
709 according to the manufacturer's instructions. After transfection, cells were plated in home-

710 made microscopy-compatible dishes and cultured for an additional 72 hours. Fixation was
711 carried out using 2% paraformaldehyde (PFA) in PBS for 15 minutes at room temperature.
712 Imaging was performed using Total Internal Reflection Fluorescence (TIRF) microscopy on a
713 Nikon Eclipse Ti system equipped with Perfect Focus System (PFS) and a 100×/1.49 NA oil
714 immersion objective, to visualize focal adhesion markers. Fluorescence images were
715 processed in FIJI (ImageJ). Individual cell outlines were manually traced to define cell
716 boundaries. A Euclidean distance map (EDM) was generated from each cell mask and the
717 distance values were normalized by the maximum radial distance of the cell to produce a
718 relative scale ranging from 0 (periphery) to 1 (center). Focal adhesions were detected with
719 an intensity threshold, followed by region of interest (ROI) creation using the "Analyze
720 Particles" function. These ROIs were overlaid onto the normalized distance maps, and the
721 mean value within each ROI was computed, representing the average position of each
722 adhesion relative to the cell center. Six cells were analyzed per condition in each experiment,
723 with three independent experimental repeats.
724 **Actin centrality analysis using total internal reflection fluorescence (TIRF) microscopy.**
725 LacZ-, and POU5F1B-expressing SW480 cells were stained with Phalloidin-iFluor 647
726 (Cayman Chemical) to visualize actin and imaged using TIRF microscopy with a Nikon Eclipse
727 Ti equipped with PFS and a 100x 1.49 NA objective. To quantify the spatial distribution of
728 actin, we used a custom MATLAB pipeline to measure fluorescence intensity along radial lines
729 from the cell centre to the periphery. In the first script, a manually defined ROI (drawn in Fiji
730 and saved as a .roi file) was used to outline cell contours. Radial intensity profiles were then
731 extracted from the centroid outward at 1° angular steps (360 directions per cell), with intensity
732 values interpolated along each line. The distances were normalized from 0(periphery)
733 to 1 (cell center), and the resulting raw and binned data (mean, SEM, and standard deviation)
734 were exported to Excel for each cell. Subsequently, interpolated radial profiles from multiple
735 cells and conditions were combined. Technical replicates (n = 6) were averaged for each
736 biological replicate (N = 3), and the mean intensity profiles, along with SEM, were calculated
737 across biological replicates for each condition. Curves were plotted as mean ± SEM across
738 the normalized radial distance.
739 **Photoactivation experiments.** Photoactivation-based experiments (FLAP). Image
740 acquisition and analysis were performed as previously described[32]. Briefly, transfected SW480
741 cells were cultured overnight on coverslips. One hour before imaging, culturing medium was
742 replaced with F12 medium (Sigma-Aldrich), supplemented with FBS, penicillin/streptomycin,
743 and glutamine. Photoactivation was performed on a Nikon A1r confocal laser scanning
744 microscope equipped with a Å~60 oil immersion objective and a 37 °C and 5% CO2 incubation
745 chamber. Laser wavelengths of 488 and 561 nm were used to acquire three pictures at 5 s
746 intervals before photoactivation and 1 frame every 2 s for 3 min after photoactivation.

747 Excitation of photoactivatable GFP molecules was achieved by means of a 405 nm laser (15%
748 power), on a single ROI matching the size of an mCherry-positive focal adhesion. Using Imaris
749 combined with MATLAB scripts, we identified the area of photoactivation, automatically
750 repositioned it in case of lateral shift according to the mCherry signal, and extracted the mean
751 green intensity within the ROI for each time point. The first three time points, corresponding
752 to the background, were averaged and subtracted from the full-time course. The intensity of
753 the first acquisition after photoactivation was set to "100% intensity" and all other values were
754 calculated as ratio. For each photoactivation time series, a constrained double decaying
755 exponentials model (decreasing form) with the formula $(\bar{F}_0 - c)\left(k_{fast}e^{-\lambda_{fast}\cdot t} + (\bar{F}_0 -$
756 $k_{fast})e^{-\lambda_{slow}\cdot t}\right) + c$ was used to fit the data points. For each of them, the half-life was defined
757 as the time needed to lose 50% of the intensity at time 0, shown in the box and whisker plot,
758 and used for statistical comparison. The same constrained double decaying exponentials
759 model was also used to fit the average data, offering a visual inspection of the goodness of
760 the fit (theoretical model). To address the heterogeneity of paxillin recruitment and stability at
761 focal adhesions, we excluded the first 6 seconds immediately after photoactivation from our
762 analysis. Previous studies suggest that focal adhesions form a shell-like structure where
763 multiple low-affinity interactions cause an initial, very short-lived recruitment phase[75].
764 Consistent with this, we observed a quickly dissipating subpopulation of paxillin leaving the
765 adhesion area right after activation. By excluding this early phase, we aimed to minimize the
766 influence of this unstable pool and focus on the more stably associated population. Evidence
767 for different paxillin subpopulations, including a membrane-associated fraction[32], supports this
768 approach, which may explain the fast-dissociating component.
769 **Spheroid assay: embedded in collagen I.** Spheroids with SW480 cells were prepared
770 following a protocol similar to the classical agarose cushion protocol[76]. We coated 96-well
771 plates with 100 µL of a polymethyl siloxane preparation (Sylgard 184, Dow Corning), and left
772 them overnight at 65°C to create a soft U-shape bottom well. Plates were sterilized by rinsing
773 them with 70% w/v ethanol in deionized water and exposed to UV lamps for 1h in a biosafety
774 cabinet (Safe 2020, Thermo Scientific). Each well was filled with 100 µL of a 5% w/v solution
775 of Pluronic® F-127 (P2443, Sigma-Aldrich) in DPBS (14190-094, Gibco) for at least 30
776 minutes, to prevent subsequent cell adhesion. After discarding the Pluronic solution, each well
777 was filled with 100 µL of culture medium containing 2000 cells. Plates were incubated at 37°C
778 and 5% CO_2 for 4 days. Spheroids were individually harvested using wide bore pipette tips
779 (Axygen), deposed on 35 mm cell-culture dish on ice, and embedded in a drop of 1.5mg/mL
780 rat tail type I collagen solution (#5153, Advanced Biomatrix) in DPBS. A 3-5 µL droplet of
781 collagen solution containing the spheroid was then pipetted at the center of a glass bottom
782 well of a 96-well plate (P96-1.5h-N, Cellvis) kept on ice. Once the whole plate was loaded with

783 dome-like droplets containing spheroids, it was inverted and kept 9 minutes in the incubator
784 at 37°C. Then the plate was put back upright at room temperature (RT) and each well filled
785 with RT growth medium containing 500 ng ml−1 doxycycline to activate transgene expression.
786 This method ensured spheroids were fully embedded at the center of a collagen droplet, away
787 from the bottom of the well. Spheroids were cultured at 37°C and 5% CO_2 for 4-5 days.
788 **Spheroid imaging and analysis.** Each spheroid was imaged at day 4 (shROCK experiment)
789 or at day 5 (POU5F1B mutants' experiment) using a Leica SP8 inverted confocal microscope
790 equipped with a motorized stage and turret, through a 25x objective (HC FLUOTAR L 25x/0,95
791 W VISIR, numerical aperture 0.95, water immersion). Excitation light was emitted by a
792 Supercontinuum White Light Laser and composed of 480nm wavelength and 670 nm
793 wavelength. Reflected and fluorescent signals were collected by the objective, filtered into two
794 bandwidths (483 to 600nm for GFP signal, and 664 to 674 for the reflected signal), each
795 captured by distinct photomultipliers. A third photomultiplier captured the transmitted light to
796 obtain an image with the light traversing the samples. Each spheroid was scanned with a
797 spatial resolution dx = dy = 0.192 µm and dz = 5µm, with a voxel dwell time of 125 ns. All
798 image acquisition was performed using the software LAS X (Leica) and images exported in
799 the native proprietary file. Images were analyzed using ImageJ (v 1.54). For each stack, the
800 contrast was enhanced (saturation of 0.35% of the pixels over the whole stack) and the
801 contour of the spheroid was segmented manually on the transmitted light images, after
802 selecting manually the slice corresponding to the median plane of the spheroid. The
803 segmentation was repeated similarly for the maximum extent of the cell evasion. Fluorescent
804 and reflected light images were used to identify the most relevant frame in ambiguous cases.
805 Spheroids that were in contact with the bottom of the wells were excluded from the analysis.
806 **Spheroid assay: in low or high viscosity medium.** Spheroids with SW480 cells were
807 generated out of one single cell as previously described[34]. Briefly, growth-factor-reduced
808 Matrigel (Corning) was diluted 1:3 with cold L15 medium supplemented with 10% FBS and
809 1% penicillin–streptomycin. 50 µl of the diluted Matrigel were transferred to each well of a 96-
810 well plate and allowed to polymerize at 37 °C and 5% CO_2 for 1 h. Cells were collected from
811 culture flasks, resuspended in diluted Matrigel and gently dispensed (2,000 cells per 50 µl) on
812 top of the previously polymerized Matrigel in each well. After incubation at 37 °C and 5% CO_2
813 for 2 h, 100 µl of L15 was added into each well. The medium was replaced every 2 days until
814 spheroids were collected for experiments 12 days later. Spheroids were collected after
815 dissolving the Matrigel in cold L15 and centrifuged at 2,000g for 5 min. After removing the
816 supernatant, spheroids were resuspended in either 0.77 or 8 cP medium and plated onto
817 collagen-I-coated (20 µg ml−1) glass bottom 96-well plates (P96-1.5h-N, Cellvis). After 60 min,
818 the spheroids were imaged every 17 min for 21 h on the PerkinElmer Operetta high throughput
819 microscope in brightfield, with a 10x air objective. Data was acquired with the Harmony 4.9

820 software. First-cell dissociation times were defined by manually recording the time required
821 for the first cell to fully detach from each intact spheroid.
822 **Low-throughput BVdU treatment curves.** SW480 cells stably transduced with bicistronic
823 lentiviruses encoding (i) DCK, or POU5F1B-DCK and (ii) GFP, as well as POU5F1B-
824 expressing and wild type SW480 control cells, were seeded into 96-well plates at 2000 cells
825 per well in 100 µL of media. The next day, 1 M BVdU dissolved in DMSO was diluted into
826 media to prepare 6× stock solutions of BVdU at concentrations of 640 mM, 320 mM, 160 mM,
827 80 mM, 40 mM and 4 mM. For each stock solution, DMSO concentration was adjusted to a
828 final concentration of 0.25%. 0.3 µL/well of the 6× stock solutions were dispensed in the 6 first
829 rows of the 96-well dish to achieve final concentrations of 1600 µM, 800 µM, 400 µM, 200 µM,
830 100 µM and 10 µM respectively. Media with 0.25% DMSO was added to the seventh row as
831 a control. Four days later, cell viability was assessed with PrestoBlue™ reagent (A13262,
832 Invitrogen) following manufacturer's instructions.
833 **High-throughput screening using the DCK*-based positive selection assay.** High-
834 throughput chemical library screening were performed as previously described[41]. Briefly,
835 POU5F1B-DCK SW480 cells were seeded into 384-well plates (Corning, #3764) at a density
836 of 750 cells per well in a volume of 30 µl of media. Plates already contained a library of 5,758
837 lyophilized known bioactive compounds, to which cells were exposed for 24 hours before
838 adding BVdU at a final concentration of 200 uM into columns 2 to 24. After 4 days, the GFP
839 fluorescence of each assay plates was quantified using an Acumen scanning laser cytometer.
840 For each plate, the average and SD of the GFP fluorescence of wells in columns 3 to 22 were
841 calculated. For each well on an assay plate, the GFP fluorescence was converted to a z score
842 using the formula: z(well) = [GFP (well) − µ GFP (plate)] / σ GFP (plate), where µ GFP (plate)
843 is the mean GFP fluorescence for that plate and σ GFP (plate) is the SD for that plate.
844 **Radiolabeling 35S-cys/met incorporation.** For metabolic labeling, transduced cells were
845 washed with methionine /cysteine free medium, incubated 20min pulse at 37°C with 50 mCi/ml
846 35S-methionine/cysteine, washed and further incubated for different times at 37 °C in complete
847 medium with a 10-fold excess of non-radioactive methionine and cysteine. Proteins were
848 immunoprecipitated and analyzed by SDS-PAGE. Autoradiography and western blot were
849 quantified using the Typhoon Imager (Image QuantTool, GE healthcare).
850
851

852 ## References
853

854 1. Susumu Ohno. *Evolution by Gene Duplication*.
855 2. McCarrey, J. R. & Thomas, K. Human testis-specific PGK gene lacks introns and possesses
856 characteristics of a processed gene. *Nature* **326**, 501–505 (1987).
857 3. Betrán, E., Thornton, K. & Long, M. Retroposed New Genes Out of the X in Drosophila.
858 *Genome Res.* **12**, 1854 (2002).
859 4. Emerson, R. O. & Thomas, J. H. Adaptive Evolution in Zinc Finger Transcription Factors.
860 *PLoS Genet.* **5**, e1000325 (2009).
861 5. Vinckenbosch, N., Dupanloup, I. & Kaessmann, H. Evolutionary fate of retroposed gene
862 copies in the human genome. *Proc. Natl. Acad. Sci. U. S. A.* **103**, 3220–3225 (2006).
863 6. Potrzebowski, L. *et al.* Chromosomal Gene Movements Reflect the Recent Origin and
864 Biology of Therian Sex Chromosomes. *PLOS Biol.* **6**, e80 (2008).
865 7. Carelli, F. N. *et al.* The life history of retrocopies illuminates the evolution of new mammalian
866 genes. *Genome Res.* **26**, 301–314 (2016).
867 8. Kubiak, M. R. & Makałowska, I. Protein-Coding Genes' Retrocopies and Their Functions.
868 *Viruses* **9**, 80 (2017).
869 9. Abegglen, L. M. *et al.* Potential Mechanisms for Cancer Resistance in Elephants and
870 Comparative Cellular Response to DNA Damage in Humans. *JAMA* **314**, 1850–1860
871 (2015).
872 10. Sulak, M. *et al.* TP53 copy number expansion is associated with the evolution of
873 increased body size and an enhanced DNA damage response in elephants. *eLife* **5**, e11994
874 (2016).
875 11. Padariya, M. *et al.* The Elephant Evolved p53 Isoforms that Escape MDM2-Mediated
876 Repression and Cancer. *Mol. Biol. Evol.* **39**, msac149 (2022).
877 12. Simó-Riudalbas, L. *et al.* Transposon-activated POU5F1B promotes colorectal cancer
878 growth and metastasis. *Nat. Commun.* **13**, 4913 (2022).
879 13. Hayashi, H. *et al.* The OCT4 pseudogene POU5F1B is amplified and promotes an
880 aggressive phenotype in gastric cancer. *Oncogene* **34**, 199–208 (2015).
881 14. Pan, Y. *et al.* POU5F1B promotes hepatocellular carcinoma proliferation by activating
882 AKT. *Biomed. Pharmacother. Biomedecine Pharmacother.* **100**, 374–380 (2018).
883 15. Chen, L. *et al.* HPV-16 E2/E6 and POU5F1B as Biomarkers to Determine Cervical
884 High-Grade Squamous Lesions and More. *J. Inflamm. Res.* **13**, 813–821 (2020).
885 16. Hu, Z. *et al.* Genome-wide profiling of HPV integration in cervical cancer identifies
886 clustered genomic hot spots and a potential microhomology-mediated integration
887 mechanism. *Nat. Genet.* **47**, 158–163 (2015).

888 17. Pickart, C. M. & Eddins, M. J. Ubiquitin: structures, functions, mechanisms. *Biochim.*
889 *Biophys. Acta BBA - Mol. Cell Res.* **1695**, 55–72 (2004).
890 18. Hyer, M. L. *et al.* A small-molecule inhibitor of the ubiquitin activating enzyme for
891 cancer treatment. *Nat. Med.* **24**, 186–193 (2018).
892 19. Levental, I., Grzybek, M. & Simons, K. Greasing Their Way: Lipid Modifications
893 Determine Protein Association with Membrane Rafts. *Biochemistry* **49**, 6305–6316 (2010).
894 20. Melkonian, K. A., Ostermeyer, A. G., Chen, J. Z., Roth, M. G. & Brown, D. A. Role of
895 Lipid Modifications in Targeting Proteins to Detergent-resistant Membrane Rafts: MANY
896 RAFT PROTEINS ARE ACYLATED, WHILE FEW ARE PRENYLATED *. *J. Biol. Chem.*
897 **274**, 3910–3917 (1999).
898 21. Anwar, M. U. *et al.* ER-Golgi-localized proteins TMED2 and TMED10 control the
899 formation of plasma membrane lipid nanodomains. *Dev. Cell* **57**, 2334-2346.e8 (2022).
900 22. Levental, I., Levental, K. R. & Heberle, F. A. Lipid Rafts: Controversies Resolved,
901 Mysteries Remain. *Trends Cell Biol.* **30**, 341–353 (2020).
902 23. Stix, R., Lee, C.-J., Faraldo-Gómez, J. D. & Banerjee, A. Structure and Mechanism of
903 DHHC Protein Acyltransferases. *J. Mol. Biol.* **432**, 4983–4998 (2020).
904 24. Leitao, S. M. *et al.* Time-Resolved Scanning Ion Conductance Microscopy for Three-
905 Dimensional Tracking of Nanoscale Cell Surface Dynamics. *ACS Nano* **15**, 17613–17622
906 (2021).
907 25. Huang, D. W., Sherman, B. T. & Lempicki, R. A. Systematic and integrative analysis
908 of large gene lists using DAVID bioinformatics resources. *Nat. Protoc.* **4**, 44–57 (2009).
909 26. Sherman, B. T. *et al.* DAVID: a web server for functional enrichment analysis and
910 functional annotation of gene lists (2021 update). *Nucleic Acids Res.* **50**, W216–W221
911 (2022).
912 27. Gross, S. P., Vershinin, M. & Shubeita, G. T. Cargo Transport: Two Motors Are
913 Sometimes Better Than One. *Curr. Biol.* **17**, R478–R486 (2007).
914 28. Hanks, S. K. & Polte, T. R. Signaling through focal adhesion kinase. *BioEssays News*
915 *Rev. Mol. Cell. Dev. Biol.* **19**, 137–145 (1997).
916 29. Wehrle-Haller, B. Structure and function of focal adhesions. *Curr. Opin. Cell Biol.* **24**,
917 116–124 (2012).
918 30. Webb, D. J. *et al.* FAK-Src signalling through paxillin, ERK and MLCK regulates
919 adhesion disassembly. *Nat. Cell Biol.* **6**, 154–161 (2004).
920 31. Mavrakis, M. & Juanes, M. A. The compass to follow: Focal adhesion turnover. *Curr.*
921 *Opin. Cell Biol.* **80**, 102152 (2023).
922 32. Ripamonti, M. *et al.* Structural and functional analysis of LIM domain-dependent
923 recruitment of paxillin to αvβ3 integrin-positive focal adhesions. *Commun. Biol.* **4**, 1–21
924 (2021).

925 33. Bera, K. *et al.* Extracellular fluid viscosity enhances cell migration and cancer
926 dissemination. *Nature* **611**, 365–373 (2022).
927 34. Rosenson, R. S., McCormick, A. & Uretz, E. F. Distribution of blood viscosity values
928 and biochemical correlates in healthy adults. *Clin. Chem.* **42**, 1189–1195 (1996).
929 35. Ito, T. *et al.* Identification of a Primary Target of Thalidomide Teratogenicity. *Science*
930 **327**, 1345–1350 (2010).
931 36. Krönke, J. *et al.* Lenalidomide causes selective degradation of IKZF1 and IKZF3 in
932 multiple myeloma cells. *Science* **343**, 301–305 (2014).
933 37. Lu, G. *et al.* The myeloma drug lenalidomide promotes the cereblon-dependent
934 destruction of Ikaros proteins. *Science* **343**, 305–309 (2014).
935 38. Lopez-Girona, A. *et al.* Cereblon is a direct protein target for immunomodulatory and
936 antiproliferative activities of lenalidomide and pomalidomide. *Leukemia* **26**, 2326–2335
937 (2012).
938 39. Zhu, Y. X. *et al.* Cereblon expression is required for the antimyeloma activity of
939 lenalidomide and pomalidomide. *Blood* **118**, 4771–4779 (2011).
940 40. Koduri, V. *et al.* Targeting oncoproteins with a positive selection assay for protein
941 degraders. *Sci. Adv.* **7**, eabd6263 (2021).
942 41. Neschadim, A. *et al.* Cell Fate Control Gene Therapy Based on Engineered Variants
943 of Human Deoxycytidine Kinase. *Mol. Ther.* **20**, 1002–1013 (2012).
944 42. Zhang, J. *et al.* NANOGP8 is a retrogene expressed in cancers. *FEBS J.* **273**, 1723–
945 1730 (2006).
946 43. Jang, H. S. *et al.* Transposable elements drive widespread expression of oncogenes
947 in human cancers. *Nat. Genet.* **51**, 611–617 (2019).
948 44. Simons, K. & Toomre, D. Lipid rafts and signal transduction. *Nat. Rev. Mol. Cell Biol.*
949 **1**, 31–39 (2000).
950 45. Greenlee, J. D., Subramanian, T., Liu, K. & King, M. R. Rafting Down the Metastatic
951 Cascade: The Role of Lipid Rafts in Cancer Metastasis, Cell Death, and Clinical Outcomes.
952 *Cancer Res.* **81**, 5–17 (2021).
953 46. Montixi, C. *et al.* Engagement of T cell receptor triggers its recruitment to low-density
954 detergent-insoluble membrane domains. *EMBO J.* **17**, 5334–5348 (1998).
955 47. Nagasato, A. I., Yamashita, H., Matsuo, M., Ueda, K. & Kioka, N. The distribution of
956 vinculin to lipid rafts plays an important role in sensing stiffness of extracellular matrix.
957 *Biosci. Biotechnol. Biochem.* **81**, 1136–1147 (2017).
958 48. Khan, A. A., Bose, C., Yam, L. S., Soloski, M. J. & Rupp, F. Physiological Regulation
959 of the Immunological Synapse by Agrin. *Science* **292**, 1681–1686 (2001).
960 49. Amano, M. *et al.* Formation of Actin Stress Fibers and Focal Adhesions Enhanced by
961 Rho-Kinase. *Science* **275**, 1308–1311 (1997).

962 50. Ballestrem, C., Hinz, B., Imhof, B. A. & Wehrle-Haller, B. Marching at the front and
963 dragging behind. *J. Cell Biol.* **155**, 1319–1332 (2001).
964 51. Hamidi, H. & Ivaska, J. Every step of the way: integrins in cancer progression and
965 metastasis. *Nat. Rev. Cancer* **18**, 533–548 (2018).
966 52. Mayor, S. & Pagano, R. E. Pathways of clathrin-independent endocytosis. *Nat. Rev.*
967 *Mol. Cell Biol.* **8**, 603–612 (2007).
968 53. Lusa, S. *et al.* Depletion of rafts in late endocytic membranes is controlled by NPC1-
969 dependent recycling of cholesterol to the plasma membrane. *J. Cell Sci.* **114**, 1893–1900
970 (2001).
971 54. Gagescu, R. *et al.* The Recycling Endosome of Madin-Darby Canine Kidney Cells Is a
972 Mildly Acidic Compartment Rich in Raft Components. *Mol. Biol. Cell* **11**, 2775–2791 (2000).
973 55. Mukherjee, S. & Maxfield, F. R. Role of membrane organization and membrane
974 domains in endocytic lipid trafficking. *Traffic Cph. Den.* **1**, 203–211 (2000).
975 56. Martinez-Outschoorn, U. E., Sotgia, F. & Lisanti, M. P. Caveolae and signalling in
976 cancer. *Nat. Rev. Cancer* **15**, 225–237 (2015).
977 57. Hetmanski, J. H. R. *et al.* Membrane Tension Orchestrates Rear Retraction in Matrix-
978 Directed Cell Migration. *Dev. Cell* **51**, 460-475.e10 (2019).
979 58. Orgaz, J. L. *et al.* Myosin II Reactivation and Cytoskeletal Remodeling as a Hallmark
980 and a Vulnerability in Melanoma Therapy Resistance. *Cancer Cell* **37**, 85-103.e9 (2020).
981 59. ROCK and JAK1 signaling cooperate to control actomyosin contractility in tumor cells
982 and stroma - Google Search.
983 https://www.google.com/search?q=ROCK+and+JAK1+signaling+cooperate+to+control+a
984 ctomyosin+contractility+in+tumor+cells+and+stroma&oq=ROCK+and+JAK1+signaling+co
985 operate+to+control+actomyosin+contractility+in+tumor+cells+and+stroma&gs_lcrp=EgZja
986 HJvbWUyBggAEEUYOTIHCAEQIRiPAjIHCAIQIRiPAtIBBzM2OGowajeoAgCwAgA&sourc
987 eid=chrome&ie=UTF-8.
988 60. Barcelo, J., Samain, R. & Sanz-Moreno, V. Preclinical to clinical utility of ROCK
989 inhibitors in cancer. *Trends Cancer* **0**, (2023).
990 61. Vennin, C. *et al.* Transient tissue priming via ROCK inhibition uncouples pancreatic
991 cancer progression, sensitivity to chemotherapy, and metastasis. *Sci. Transl. Med.* **9**,
992 eaai8504 (2017).
993 62. Hartmann, S., Ridley, A. J. & Lutz, S. The Function of Rho-Associated Kinases ROCK1
994 and ROCK2 in the Pathogenesis of Cardiovascular Disease. *Front. Pharmacol.* **6**, 276
995 (2015).
996 63. Fellmann, C. *et al.* An optimized microRNA backbone for effective single-copy RNAi.
997 *Cell Rep.* **5**, 1704–1713 (2013).

998 64. Harder, T., Scheiffele, P., Verkade, P. & Simons, K. Lipid Domain Structure of the
999 Plasma Membrane Revealed by Patching of Membrane Components. *J. Cell Biol.* **141**,
1000 929–942 (1998).
1001 65. Werno, M. W. & Chamberlain, L. H. S-acylation of the Insulin-Responsive
1002 Aminopeptidase (IRAP): Quantitative analysis and Identification of Modified Cysteines. *Sci.*
1003 *Rep.* **5**, 12413 (2015).
1004 66. Nečas, D. & Klapetek, P. Gwyddion: an open-source software for SPM data analysis.
1005 *Open Phys.* **10**, 181–188 (2012).
1006 67. Sergeeva, O. A. & van der Goot, F. G. Anthrax toxin requires ZDHHC5-mediated
1007 palmitoylation of its surface-processing host enzymes. *Proc. Natl. Acad. Sci. U. S. A.* **116**,
1008 1279–1288 (2019).
1009 68. Cox, J. & Mann, M. MaxQuant enables high peptide identification rates, individualized
1010 p.p.b.-range mass accuracies and proteome-wide protein quantification. *Nat. Biotechnol.*
1011 **26**, 1367–1372 (2008).
1012 69. Shin, J. *et al.* Use of Composite Protein Database including Search Result Sequences
1013 for Mass Spectrometric Analysis of Cell Secretome. *PLOS ONE* **10**, e0121692 (2015).
1014 70. Zhang, X. *et al.* Proteome-wide identification of ubiquitin interactions using UbIA-MS.
1015 *Nat. Protoc.* **13**, 530–550 (2018).
1016 71. Ritchie, M. E. *et al.* limma powers differential expression analyses for RNA-sequencing
1017 and microarray studies. *Nucleic Acids Res.* **43**, e47 (2015).
1018 72. Wiśniewski, J. R., Zougman, A., Nagaraj, N. & Mann, M. Universal sample preparation
1019 method for proteome analysis. *Nat. Methods* **6**, 359–362 (2009).
1020 73. Kulak, N. A., Pichler, G., Paron, I., Nagaraj, N. & Mann, M. Minimal, encapsulated
1021 proteomic-sample processing applied to copy-number estimation in eukaryotic cells. *Nat.*
1022 *Methods* **11**, 319–324 (2014).
1023 74. Wolfenson, H. *et al.* A Role for the Juxtamembrane Cytoplasm in the Molecular
1024 Dynamics of Focal Adhesions. *PLOS ONE* **4**, e4304 (2009).
1025 75. Dolega, M. E. *et al.* Cell-like pressure sensors reveal increase of mechanical stress
1026 towards the core of multicellular spheroids under compression. *Nat. Commun.* **8**, 14056
1027 (2017).
1028

Figure 1

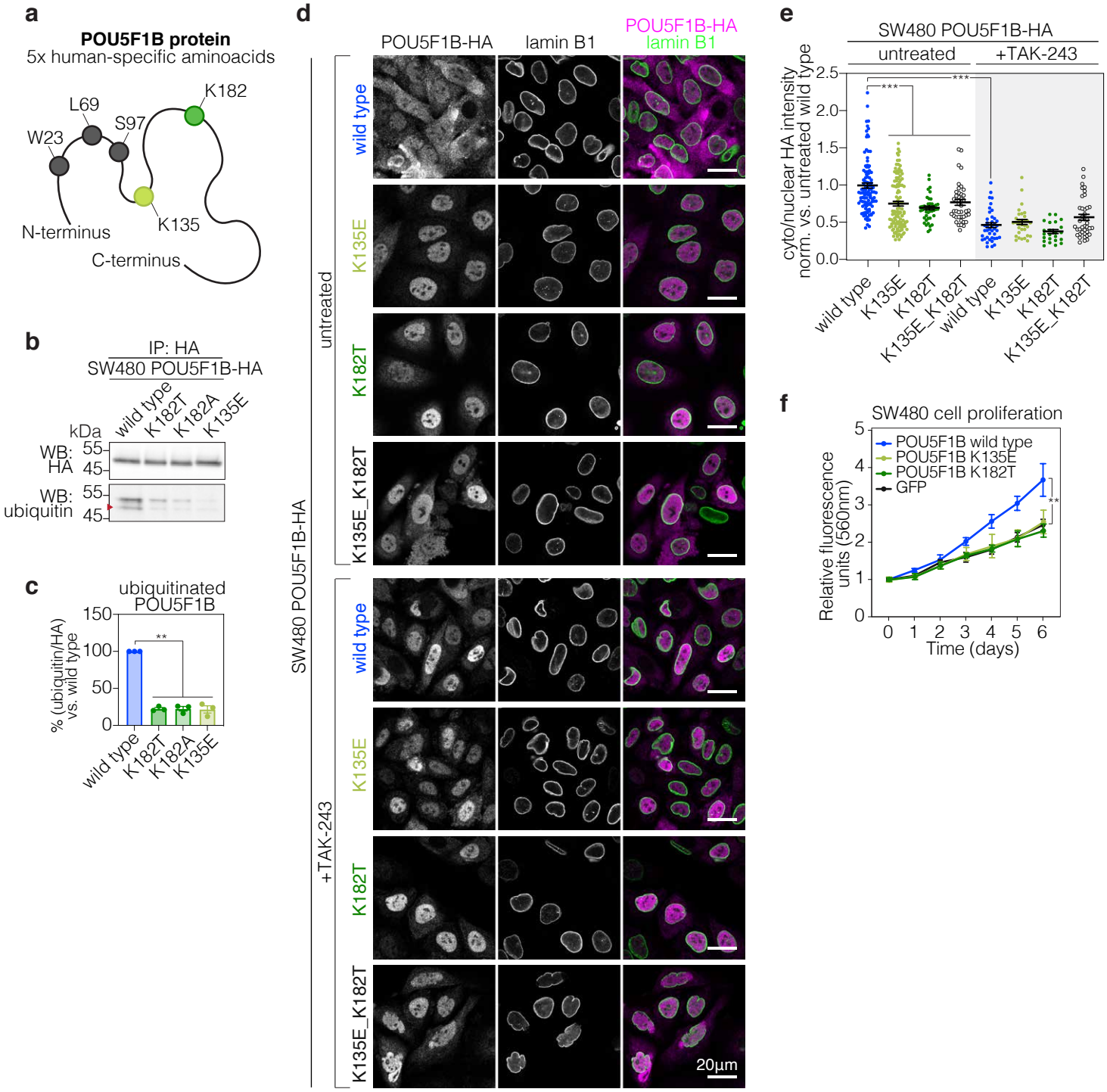

Figure 1. POU5F1B cytoplasmic localization and growth-stimulating effects depend on ubiquitination of human-restricted lysine residues. a, Schematic representation of human POU5F1B (359 aa) protein, with the five human-specific amino acids highlighted. K135 and K182 in green are focus of our study. **b,** Immunoprecipitation (IP) and western blot (WB) analysis of HA-tagged wild type (WT)-, K182T-, K182A-, and K135E-POU5F1B in SW480 cells. **c,** Quantification of western blot bands shown in (b) (wild type vs. K182T P=5.1e-04; vs. K182A P=1.6e-03; vs. K135E P=3.9e-03 by t-test). **d,** Representative immunofluorescence-confocal microscopy of untreated and TAK-243 (1uM, 5h) treated POU5F1B-HA wild type-, K135E-, K182T-, K135E-K182T-overexpressing SW480 cells, with HA in magenta and the nuclear membrane marker lamin-B1 in green. **e,** Ratio cytoplasm/nucelus of HA signal intensity from cells presented in (d). Each data point was normalized to the mean intensity of untreated POU5F1B-HA wild type cells (untreated wild type vs. K135E P=4.4e-07; vs. K182T P=2.43e-08; vs. K135E_K182T P=6.42e-05; vs. TAK243 wild type P=1.12e-15 by Wilcoxon test). **f,** PrestoBlue cell proliferation assay in POU5F1B-wild type-, -K135E-, -K182T-, and GFP-overexpressing SW480 cells. (n = 3 independent experiments, P = 0.001 by Wilcoxon test). ** pvalue<0.01, *** pvalue<0.001.

Figure 2

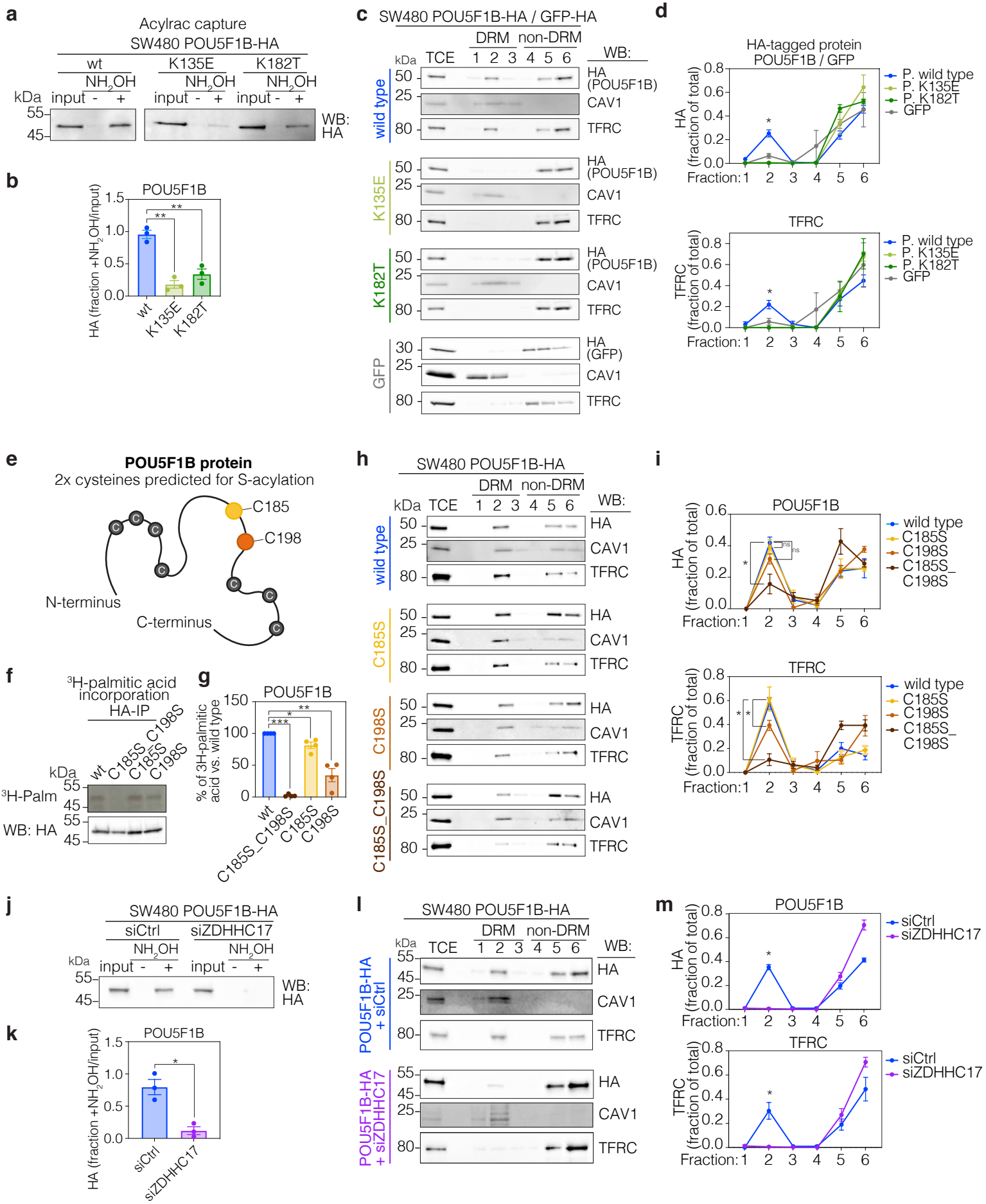
a
Acylrac capture
SW480 POU5F1B-HA
wt
K135E
K182T
NH2OH
kDa input - +
55
45
WB: HA
b
POU5F1B
HA (fraction +NH2OH/input)
1.5
1.0
0.5
0.0
**
**
wt
K135E
K182T
c
SW480 POU5F1B-HA / GFP-HA
DRM non-DRM
kDa TCE 1 2 3 4 5 6
WB:
wild type
K135E
K182T
GFP
50
25
80
30
HA (POU5F1B)
HA (GFP)
CAV1
TFRC
d
HA-tagged protein
POU5F1B / GFP
HA (fraction of total)
TFRC (fraction of total)
Fraction: 1 2 3 4 5 6
P. wild type
P. K135E
P. K182T
GFP
e
POU5F1B protein
2x cysteines predicted for S-acylation
C185
C198
N-terminus
C-terminus
f
3H-palmitic acid incorporation
HA-IP
wt
C185S_C198S
C185S
C198S
kDa
3H-Palm
WB: HA
55
45
g
POU5F1B
% of 3H-palmitic acid vs. wild type
150
100
50
0
***
*
**
wt
C185S_C198S
C185S
C198S
h
SW480 POU5F1B-HA
DRM non-DRM
kDa TCE 1 2 3 4 5 6
WB:
wild type
C185S
C198S
C185S_C198S
50
25
80
HA
CAV1
TFRC
i
POU5F1B
TFRC
HA (fraction of total)
TFRC (fraction of total)
Fraction: 1 2 3 4 5 6
ns
wild type
C185S
C198S
C185S_C198S
j
SW480 POU5F1B-HA
siCtrl
siZDHHC17
NH2OH
kDa input - + input - +
55
45
WB: HA
k
POU5F1B
HA (fraction +NH2OH/input)
1.5
1.0
0.5
0.0
*
siCtrl
siZDHHC17
l
SW480 POU5F1B-HA
DRM non-DRM
kDa TCE 1 2 3 4 5 6
WB:
POU5F1B-HA + siCtrl
POU5F1B-HA + siZDHHC17
55
45
25
80
HA
CAV1
TFRC
m
POU5F1B
TFRC
HA (fraction of total)
TFRC (fraction of total)
Fraction: 1 2 3 4 5 6
siCtrl
siZDHHC17

Figure 2. ZDHHC17-mediated acylation is necessary for POU5F1B action on membrane nanodomains. a, Acylrac capture assay in POU5F1B-HA wild type-, K135E-, K182T-overexpressing SW480 cells. Western blot (WB) anti-HA of total cell extracts (input), S-acylated (plus hydroxylamine +NH_2OH) and control fractions (–NH_2OH). **b,** Ratio of HA signal in S-acylated fraction/total cell extracts from three independent acylrac experiments (wild type vs. K135E P=0.001; vs. K182T P=0.004 by t-test). **c,** Isolation of detergent-resistant membranes (DRMs) from POU5F1B-HA-wild type-, -K135E-, -K182T-, and GFP-overexpressing SW480 cells. 1-3 correspond to insoluble fractions, 4-6 to soluble fractions, DRMs being traditionally found in fraction 2. Caveolin1 (CAV1) and transferrin receptor (TFRC) are used as controls for insoluble and soluble fractions, respectively (representative blot out of three independent experiments). **d,** Quantification of western blot in (c) normalized within each experiment (Fraction 2 in HA blot: wild type vs. K135E P=0.013; vs. K182T P=0.012; vs. GFP P=0.009; fraction 2 in TFRC blot: wild type vs. K135E P=0.035; vs. K182T P=0.030; vs. GFP P=0.040 by t-test). **e,** Schematic representation of human POU5F1B protein, with the nine cysteines highlighted. C198 is predicted for S-aclyation by SwissPalm and C185 by physical proximity to C198. **f,** Autoradiography (^{3}H-Palm) and WB of immunoprecitated HA-tagged wild type (wt)-, C185S_C198S-, C185S-, C198S-POU5F1B in ^{3}H-palmitic acid-labeled SW480 cells. **g,** Quantification of bands in (f) (n=3 independent experiments; P=2.38e-06, P=0.034, P=0.008, respectively, by t-test). **h,** Isolation of DRMs from cells in (f). **i,** Quantification of western blot bands in (h) (Fraction 2 in POU5F1B blot: POU5F1B wild type vs. C185S P=0.65 ; vs. C198S P=0.079 ; vs. C185S_C198S P=0.015; fraction 2 in TFRC blot: POU5F1B wild type vs. C185S P=0.765 ; vs. C198S P=0.048 ; vs. C185S_C198S P=0.025 by t-test). **j,** Acylrac capture assay in siCtrl-, and siZDHHC17- POU5F1B-HA SW480 cells. **k,** Quantification of blot in (j) (P=0.014 by t-test). **l,** Isolation of DRMs from cells in (j). **m,** Quantification of western blot bands in (l) (Fraction 2 in POU5F1B blot P=0.002; fraction 2 in TFRC blot P=0.049 by t-test). ns, not significant, * pvalue<0.05, ** pvalue<0.01, *** pvalue<0.001

Figure 3

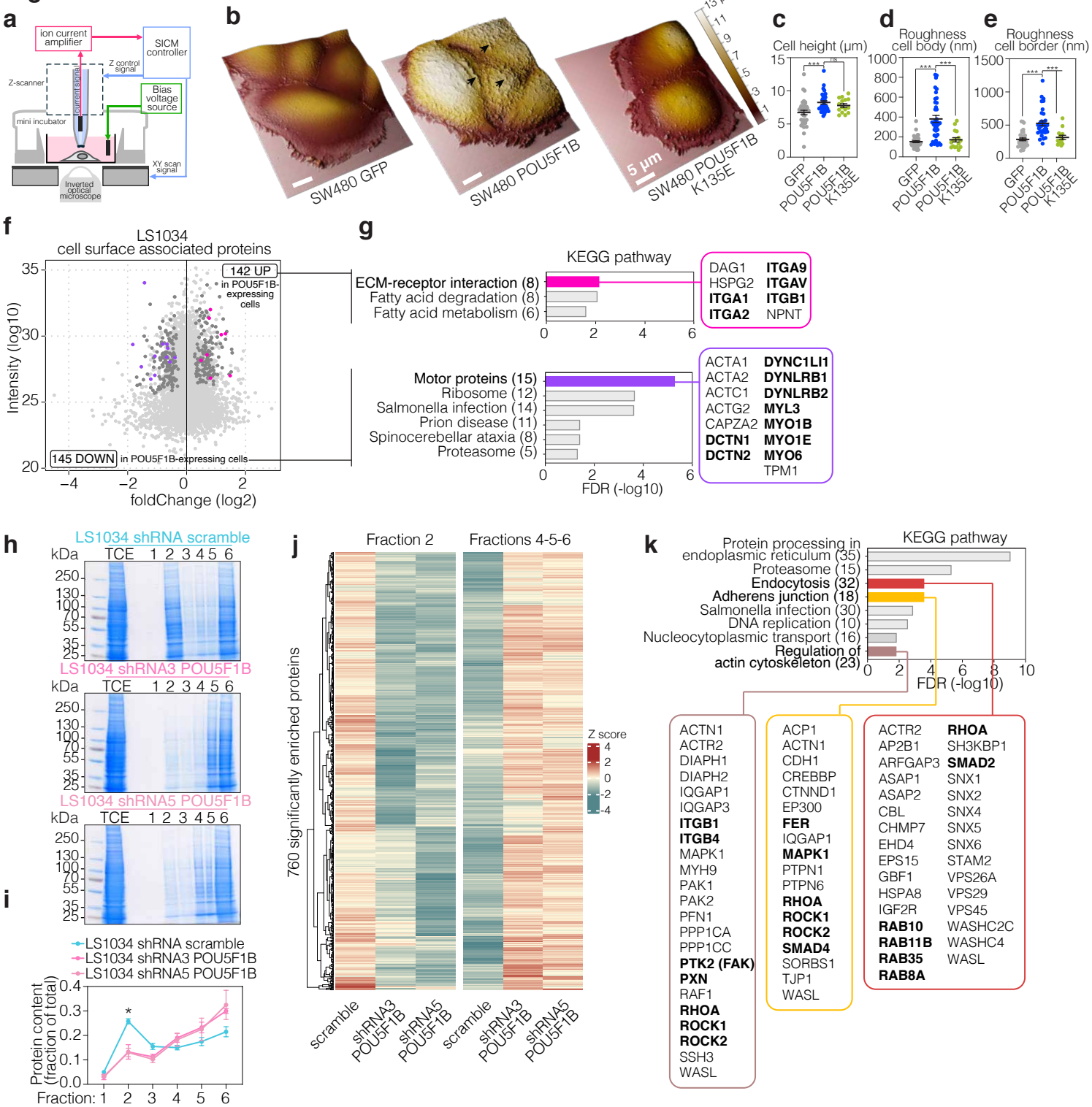

Figure 3. POU5F1B triggers the redistribution of cell adhesion proteins and changes in cell morphology. a, Scheme ilustrating the scanning ion conductance microscopy (SICM) tehcnique to study the surface morphology of cells. **b,** Representative SICM 3D images showing cell topography from GFP-, POU5F1B- and POU5F1B-K135E-expressing SW480 cells. Color scale from 0 to 13 µm reveals cell heigth values. Black arrows indicate protrusions projected upward in the z axis. **c,** Cell height (µm) (POU5F1B vs. GFP P=0.0005; vs. K135E P=0.35 by Wilcoxon test), **d,** roughness of cell body (nm) (POU5F1B vs. GFP P=1.42e-07; vs. K135E P=0.0002 by Wilcoxon test), **e,** and roughness of cell border (nm) (POU5F1B vs. GFP P=3.63e-07; vs. K135E P=0.0001 by Wilcoxon test) from cells in b. **f,** MA plot depicting relative abundance and average intensity of individual proteins identified by mass spectrometry from cell surface-associated proteins of sh-scramble vs. shRNA3 & shRNA5 LS1034 cells. Measurements were performed in independent triplicates, each dot represents a detected protein, with significantly changed ones (P < 0.05, outlier detection test as computed by MaxQuant) in dark grey and their numbers indicated in upper corners. **g,** Significantly enriched proteins were clustered in KEGG annotations using the Functional Annotation Chart from DAVID bioinformatics resources 6.8. In bold, proteins mentioned in the text. **h,** Isolation of detergent-resistant membranes (DRMs) from sh-scramble, shRNA3 & shRNA5 LS1034 cells, fractions were run on SDS-PAGE and gels were stained with Coomassie. **i,** Quantification of coomassie staining in (c) (Fraction 2 sh-scramble vs. shRNA3 P=0.018; vs. shRNA5 P=0.015 by t-test). **j,** Heatmap of mass spectrometry spectral counts from fraction 2 (F2) and fractions 4, 5, and 6 (F456), extracted from cells in (h). **k,** Significantly enriched proteins in F2 shRNA-scramble were clustered as in (g). In bold, proteins mentioned in the text. ns not significant, * pvalue<0.05, *** pvalue<0.001.

Figure 4

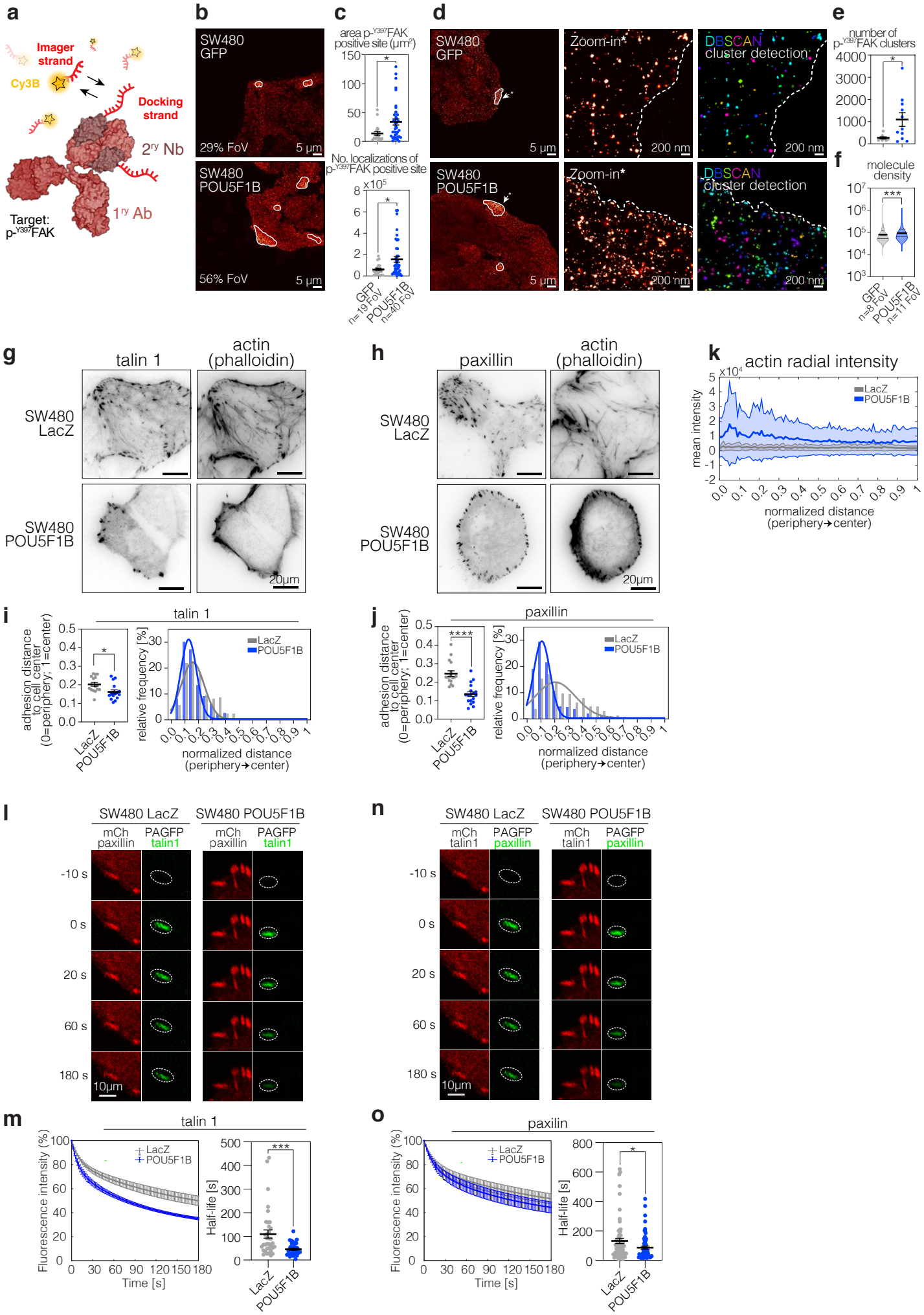
a
Imager strand
Cy3B
Docking strand
2ry Nb
1ry Ab
Target: p-Y397FAK
b
SW480 GFP
29% FoV
5 µm
SW480 POU5F1B
56% FoV
5 µm
c
area p-Y397FAK positive site (µm²)
No. localizations of p-Y397FAK positive site
x10⁵
GFP n=19 FoV
POU5F1B n=40 FoV
d
SW480 GFP
Zoom-in*
DBSCAN cluster detection
5 µm
200 nm
SW480 POU5F1B
e
number of p-Y397FAK clusters
f
molecule density
GFP n=8 FoV
POU5F1B n=11 FoV
g
talin 1
actin (phalloidin)
SW480 LacZ
SW480 POU5F1B
20µm
h
paxillin
actin (phalloidin)
k
actin radial intensity
x10⁴
mean intensity
LacZ
POU5F1B
normalized distance (periphery→center)
i
talin 1
adhesion distance to cell center (0=periphery; 1=center)
relative frequency [%]
normalized distance (periphery→center)
j
paxillin
l
SW480 LacZ
SW480 POU5F1B
mCh paxillin
PAGFP talin1
-10 s
0 s
20 s
60 s
180 s
10µm
n
mCh talin1
PAGFP paxillin
m
talin 1
Fluorescence intensity (%)
Time [s]
Half-life [s]
o
paxilin

Figure 4. POU5F1B promotes the nano-clustering, surface redistribution and increased turnover of focal adhesion proteins. a, Scheme of DNA-PAINT technique targeting p-^{Y397}FAK protein. Birefly, p-^{Y397}FAK is labeled with a primary antibody (1ry Ab) preincubated with secondary nanobody (Nb) fused to a DNA-PAINT docking sequence (red). For readout, a complementary dye-labeled (Cy3B) imager strand is added. **b,** Representative p-^{Y397}FAK-targeting DNA-PAINT images from GFPcontrol- and POU5F1B-overexpressing SW480 cells. Percentage of positive field of views (FoV) (b), area (P=0.016 by t-test) and number of localizations (P=0.026 by t-test) (**c**) are depicted. **d,** Same as in b, with a zoom in selected positive regions, and DBSCAN spatial clustering detection for extraction of cluster number (**e**) (P=0.023 by t-test) and molecule density (**f**) (P=4.6e-07 by t-test). Dashed line defines the cell boundary. **g,** Representative total internal reflection fluorescence (TIRF) microscopy of mCherry_talin1, (**h**) mCherry_paxillin and corresponding phalloidin-stained actin (**g,h**) in POU5F1B- and LacZ-overexpressing SW480 cells. **i, j,** Quantification of adhesion distance to the cell center (0=periphery, 1=center) (talin 1 P=0.01; paxillin P<0.0001 by t-test) and relative frequency signal from images in g-h. **k,** Mean actin radial intensity +/- standard deviation calculated from the cell periphery (0) to the center (1) from images in g-h. Six technical replicates from 3 biological replicates are represented in i-j-k. **l,** Representative images from experimental dissociation kinetics of PA-GFP_talin1 from mCherry_paxilin-positive FAs and **n,** photoactivable(PA)-GFP_paxilin from mCherry_talin1-positive FAs in the same cells as in g-h. **m, o,** Dissociation kinetics plots and box plot of the half-lives (talin 1 P=0.0008; paxillin P=0.028 by t-test) from images in l-n. Data from 4 independent experiments are represented in m-o. *$p \leq 0.05$; **$p < 0.01$; ***$p < 0.001$; ****$p < 0.0001$.

Figure 5

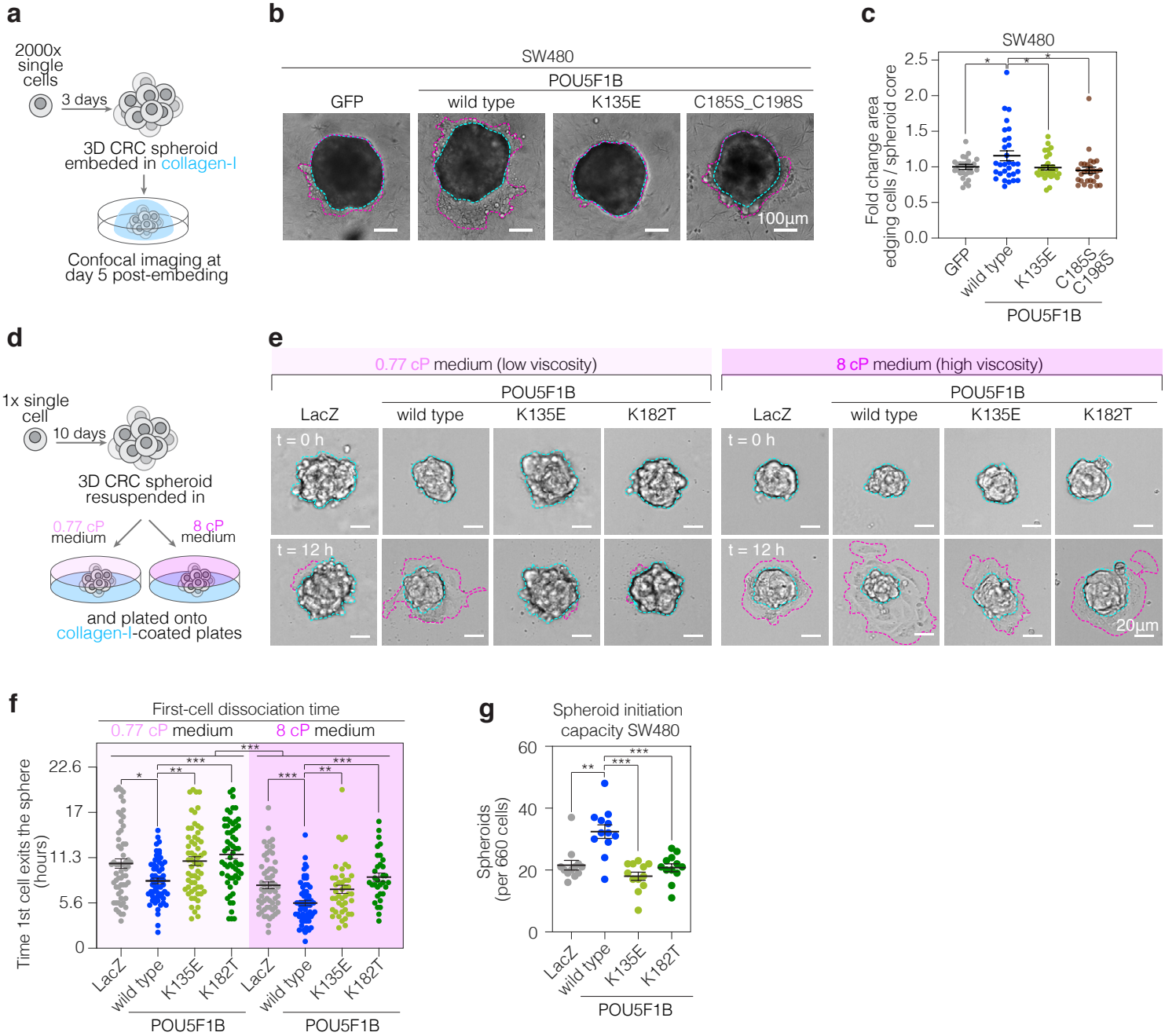

Figure 5. POU5F1B drives spontaneous cell invasion in 3D. a, Scheme ilustrating the preparation of 3D CRC spheroids embeded in collagen-I. **b,** Representative reflection contrast microscopy images of GFP-, POU5F1B-, POU5F1B-K135E-, POU5F1B-C185S_C198S-expressing SW480 spheroids. **c**, Fold change area of invading cells (in fucsia panel b) versus area spheroid core (in turquoise panel b) from spheroids in b (POU5F1B wild type vs. GFP P=0.031; vs. K135E P=0.037; vs. C185S_C198S P=0.017 by Wilcoxon test). **d,** Scheme ilustrating the preparation of 3D CRC spheroids plated onto collagen-I-coated plates and resuspended in 0.77 cP (low visocsity) and 8 cP (high viscosity) medium. **e,** Representative bright field confocal images from cells disseminating (fucsia contour) from LacZ-, POU5F1B-, POU5F1B-K135E-, POU5F1B-K182T-expressing SW480 3D spheroids (turquoise contour) cultured in low viscosity and high viscosity medium. **f,** The time required from the first cell to dissociate from each spheroid in panel e (n=60) from 3 experiments in low and high viscosity mediums (0.77 cP vs. 8 cP: LacZ vs. LacZ P=0.0009; POU5F1B vs. POU5F1B P= 8.57e-08; K135E vs. K135E P=9.57e-06; K182T vs. K182T P=0.0006. 0.77 cP experiment: POU5F1B vs. LacZ P=0.018; vs. K135E P=0.001; vs. K182T P=5.04e-06; 8 cP experiment: POU5F1B vs. LacZ P=0.0001; vs. K135E P=0.005; vs. K182T 1.57e-06 by Wilcoxin test). **g,** Number of spheroids grown from 660 LacZ-, POU5F1B-, POU5F1B-K135E-, POU5F1B-K182T-expressing SW480 single cells (POU5F1B wild type vs. LacZ P=0.003; vs. K135E P=0.0002; vs. K182T P=0.0006 by Wilcoxon test). * pvalue<0.05, ** pvalue<0.01, *** pvalue<0.001.

Figure 6

a

Protein degradation assay
Vector scheme

b

Protocol

Add drug library in 384-well plates
Plate cells
24h incubation
Add BVdU
5-day incubation
Quantify fluorescence: cell viability

c

Protein degradation assay Part I:
5,758 compounds, 1 cell line
SW480 POU5F1B-DCK

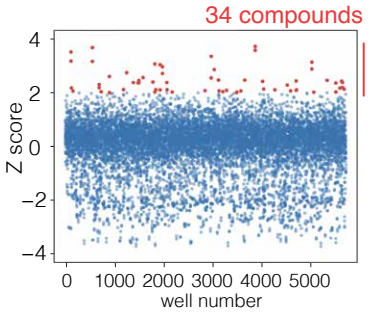

d

Protein degradation assay Part II:
dose response curve, 3 cell lines

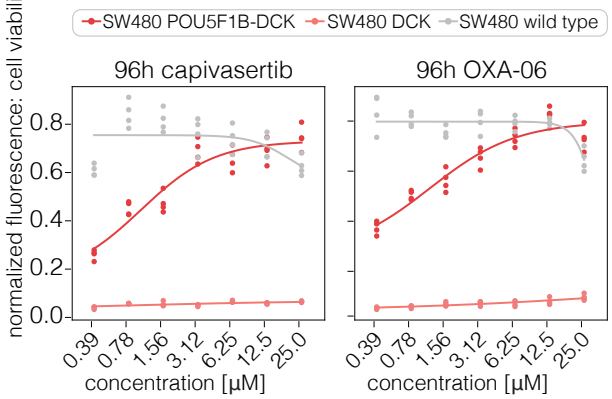

e

^{35}S Cys/Met pulsechase
SW480 POU5F1B

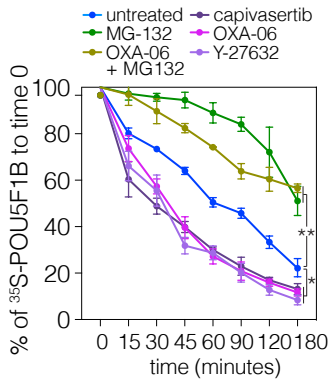

f

^{35}S Cys/Met pulsechase
SW480 POU5F1B

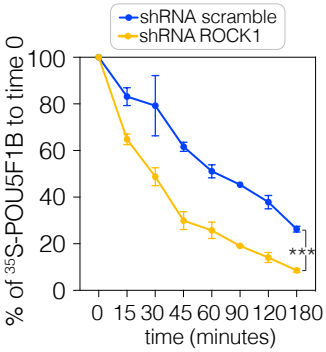

g

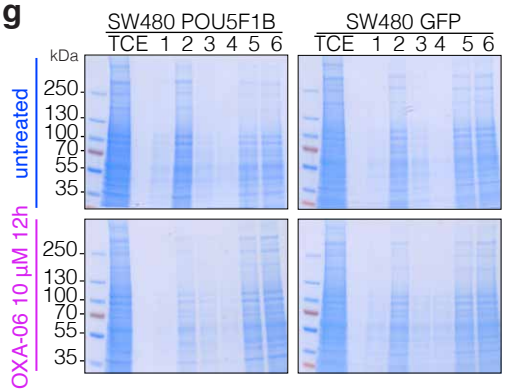

h

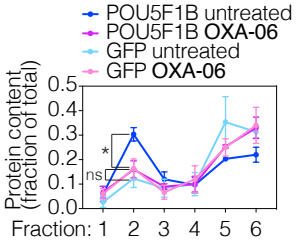

i

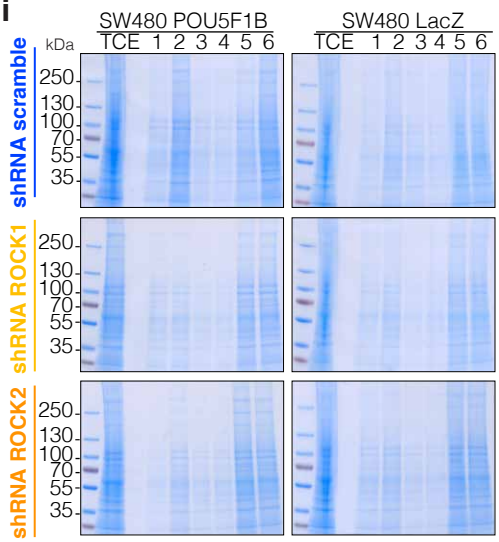

j

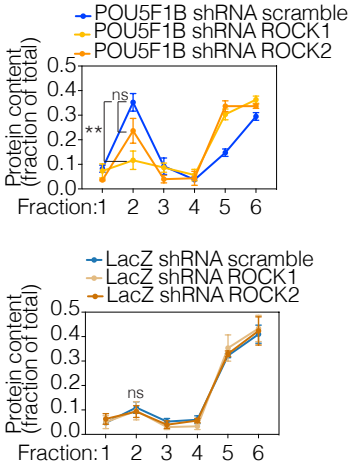

k

SW480

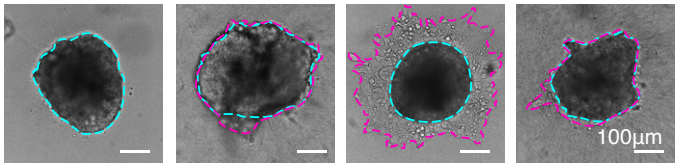

l

SW480

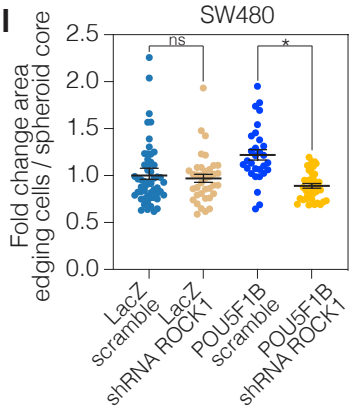

m

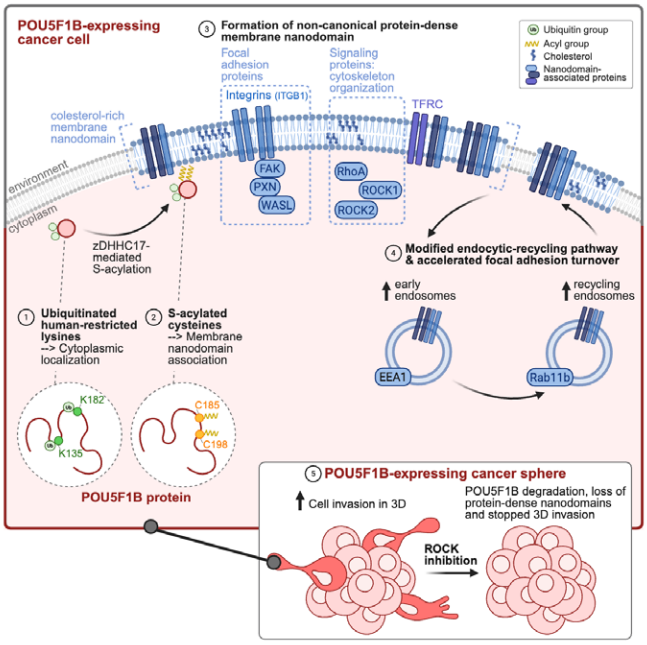

Figure 6. Loss of ROCK activity abrogates POU5F1B function. a, Vector scheme. DCK, deoxycytidine kinase; GGS, Gly-Gly-Ser spacer; IRES, internal ribosomal entry site. **b,** Protein degradation assay protocol. **c,** Z-distribution of GFP fluorescence of SW480 POU5F1B-DCK cells screened with the 5,758 known bioactive compounds library, and treated with 200uM BvdU 24h later. GFP signal was measured 48h post BvdU treatment. Colored in red, 34 compounds with a Z-score greater than the mean of the negative controls plus three standard deviations **d,** Dose response curves in wild type, POU5F1B-DCK-, and DCK-expressing SW480 cells treated with increasing concentrations of capivasertib and OXA-06 ROCK inhibitors. **e,** Pulse-chase experiment with 35SCys/Met in POU5F1B-expressing SW480 cells untreated or treated with MG-132 (10uM), OXA-06 (20uM), OXA-06 & MG-132, capivasertib (20uM), and Y-27632 (10uM). Drugs were added at time 0 and POU5F1B-HA protein was IP-ed from harvested cell pellets at indicated times (at time 180, untreated vs. MG-132 P=0.004; vs. OXA-06 P=0.026; vs. OXA-06 & MG-132 P=0.0011; vs. capivasertib P=0.03; vs. Y-27632 P=0.01 by t-test). **f,** Same as in (e) using SW480 POU5F1B cells expressing sh-scramble or sh-ROCK1 (P=0.0001 by t-test). **g,** Isolation of detergent-resistant membranes (DRMs) from POU5F1B-HA-wild-type-, and GFP-overexpressing SW480 cells untreated or treated with OXA-06 10 μM, fractions were run on SDS-PAGE and gels were stained with Coomassie. 1-3 correspond to insoluble fractions, 4-6 to soluble fractions, DRMs being traditionally found in fraction 2. **h,** Quantification of coomassie staining in (g) (POU5F1B untreated vs. POU5F1B OXA-06 P=0.02; GFP untreated vs. GFP OXA-06 P=0.95 by t-test). **i,** Same as in (g) from SW480 POU5F1B or SW480 GFP cells expressing either sh-scramble or sh-ROCK1/2. **j,** Quantification of coomassie staining in (i) (POU5F1B shRNA scramble vs. shROCK1 P=0.007; vs. shROCK2 P=0.13; LacZ shRNA scramble vs. shROCK1 P=0.77; vs shROCK2 P=0.64 by t-test). **k,** Representative reflection contrast microscopy images of 3D SW480 spheroids embeded in collagen-I, as in Figure 5a/b. **l,** Fold change area of invading cells (in fucsia panel k) versus area spheroid core (in blue panel k) from LacZ scramble-, LacZ shRNA ROCK1-, POU5F1B scramble-, and POU5F1B shRNA ROCK1-expressing SW480 spheroids (LacZ scramble vs. shROCK1 P=0.99; POU5F1B scramble vs. shROCK1 P=1.32e-06 by Wilcoxon test). ns not significant, * pvalue<0.05, ** pvalue<0.01. **m,** Model. (1) Ubiquitination of K135 and K182 human-restricted lysines retains POU5F1B protein in the cytoplasm of cancer cells. (2) S-acylation of C185 and C198 cysteines by ZDHHC17 S-acyltransferase associates POU5F1B to cholesterol-rich membrane nanodomains. (3) POU5F1B induces the formation of transferrin receptor(TFRC)-containing non-canonical protein-dense membrane nanodomains, enriched in focal adhesion (integrins -ITGB1-, FAK, PXN, WASL) and signaling proteins involved in cytoskeleton organization (RhoA, ROCK1, ROCK2). (4) POU5F1B-expressing cells present modified endocytic-recycling pathway and accelerated turnover of focal adhesion structures. Higher number of EEA1-positive early endosomes and Rab11b-positive recycling endosomes is representative of these cells. (5) POU5F1B-expressing cancer spheres present augmented cell invasiveness in 3D. ROCK inhibition triggers POU5F1B degradation, loss of protein-dense nanodomains and stops 3D invasion. Created with Biorender.com.

Supplementary Figure 1

a

```
human_POU5F1        MAGHLASDFAFSPPPGGGGDGPGGPEPGWVDPRTWLSFQGPPGGPGIGPGVGPGSEVWGI  60
human_POU5F1B       MAGHLASDFAFSPPPGGGGDGPWGAEPGWVDPLTWLSFQGPPGGPGIGPGVGPGSEVWGI  60
gorilla_POU5F1B     MAGHLASDFAFSPPPGGGGDGPGGTEPGWVDPLTWLSFQGPPGGPGIGPGAGPGSEVWGI  60
orangutan_POU5F1B   MAGHLASDFAFSPPPGGGGDGPGGTEPGWVDPLTWLSFQGPPGGPGIGPGAGPGSEVWGI  60
chimpanzee_POU5F1B  MAGHLASDFAFSPPPGGEGDGPGGPEPGWVDPLTWLRFQGPPGGPGIGPGVGPGSEVWGI  60
                    ***************** **** * ******* *** *************.*********

human_POU5F1        PPCPPPYEFCGGMAYCGPQVGVGLVPQGGLETSQPEGEAGVGVESNSDGASPEPCTVTPG  120
human_POU5F1B       PPCPPPYELCGGMAYCGPQVGVGLVPQGGLETSQPESEAGVGVESNSNGASPEPCTVPPG  120
gorilla_POU5F1B     PPCPPPYEFCRGMAYCGPQVGVGLVPQGGLETSQPEGEAGVGVESNSNGASPEPCTVPPG  120
orangutan_POU5F1B   PPCPPPYEFCRGMAYCGPQVGVGLVPQGGLETSQPEGEAGVGVESNSNGASPEPCTVPPG  120
chimpanzee_POU5F1B  PPCPPPYEFCGGMAYCGPQVGAGLVPQGGLETSQPEGEAGVGVESNSDGASPEPCTVPPG  120
                    ********:* **********.**************.**********:********* **

human_POU5F1        AVKLEKEKLEQNPEESQDIKALQKELEQFAKLLKQKRITLGYTQADVGLTLGVLFGKVFS  180
human_POU5F1B       AVKLEKEKLEQNPEKSQDIKALQKELEQFAKLLKQKRITLGYTQADVGLILGVLFGKVFS  180
gorilla_POU5F1B     AVKLEKEKLEQNP-ESQDIKALQKELEQFAKLLKQKRITLGYTQADVGLILGVLFGKVFS  179
orangutan_POU5F1B   AVKLEKEKLEQNP-ESQDIKALQKELEQFAKLLKQKRITLGYTQADVGLILGVLFGKVFS  179
chimpanzee_POU5F1B  AVKLEKEKLEQNPEESQDIKALQKELEQFAKLLKQKRITLGYTQADVGLILGVLFGKVFS  180
                    ************* :********************************* **********

human_POU5F1        QTTICRFEALQLSFKNMCKLRPLLQKWVEEADNNENLQEICKAETLVQARKRKRTSIENR  240
human_POU5F1B       QKTICRFEALQLSFKNMCKLRPLLQKWVEEADNNENLQEICKAETLMQARKRKRTSIENR  240
gorilla_POU5F1B     QTTICCFEALQLSFKNMCKLRPLLQKWVEEADNNENLQEICKAESLMQARKRKRTSIENR  239
orangutan_POU5F1B   QTTICCFEALQLSFKNMCKLRPLLQKWVEEADNNENLQEICKAESLMQARKRKRTSIENR  239
chimpanzee_POU5F1B  QTTICRFEALQLSFKNMCKLRPLLQKWVEETDNNENLQEICKAETLMQARKRKRTSIENR  240
                    *.*** ************************:*************:*:*************

human_POU5F1        VRGNLENLFLQCPKPTLQQISHIAQQLGLEKDVVRVWFCNRRQKGKRSSSDYAQREDFEA  300
human_POU5F1B       VRGNLENLFLQCPKPTL-QISHIAQQLGLEKDVVRVWFCNRRQKGKRSSSDYAQREDFEA  299
gorilla_POU5F1B     VRGNLENLFLQCPKPTL-QISHIAQQLGLEKDVVRVWFCNRRQKGKRSSSDYAQREDFEA  298
orangutan_POU5F1B   VRGNLENLFLQCPKPTL-QISHIAQQLGLEKDVVRVWFCNRRQKGKRSSSDYAQREDFEA  298
chimpanzee_POU5F1B  VRGNLENLFLQCPKPTL-QISHIAQQLGLEKDVVRVWFCNRRQKGKRSSSDYEQREDFEA  299
                    ***************** ********************************** *******

human_POU5F1        AGSPFSGGPVSFPLAPGPHFGTPGYGSPHFTALYSSVPFPEGEAFPPVSVTTLGSPMHSN  360
human_POU5F1B       AGSPFSGGPVSFPPAPGPHFGTPGYGSPHFTALYSSVPFPEGEVFPPVSVITLGSPMHSN  359
gorilla_POU5F1B     AGSPFSGGPVSFPPAPGPHFGTPGYGSPHFTALYSSVPFPEGEVFPPVSVITLGSPMHSN  358
orangutan_POU5F1B   AGSPFSGGPVSFPPAPGPHFGTPGYGSPHFTALYSSVPFPEGEVFPPVSVITLGSPMHSN  358
chimpanzee_POU5F1B  AGSPFSGGPVSFPLAPGPHFGTPGYGSPHFTALYSSVPFPEGEVFPPVSVITLGSPMHLN  359
                    ************* ****************************.****** ******* *
```

Supplementary Figure 1. Comparing POU5F1 and POU5F1B. a, Amino acid sequence alignment of human POU5F1 (360 aa), human POU5F1B (359 aa), and POU5F1B from gorilla, organgutan and chimpanzee POU5F1B (358, 358 and 359 aa respectively). POU5F1/OCT4 and POU5F1B differ by 15 residues (in pink), 5 of which are unique to human POU5F1B (pink arrows).

Supplementary Figure 2

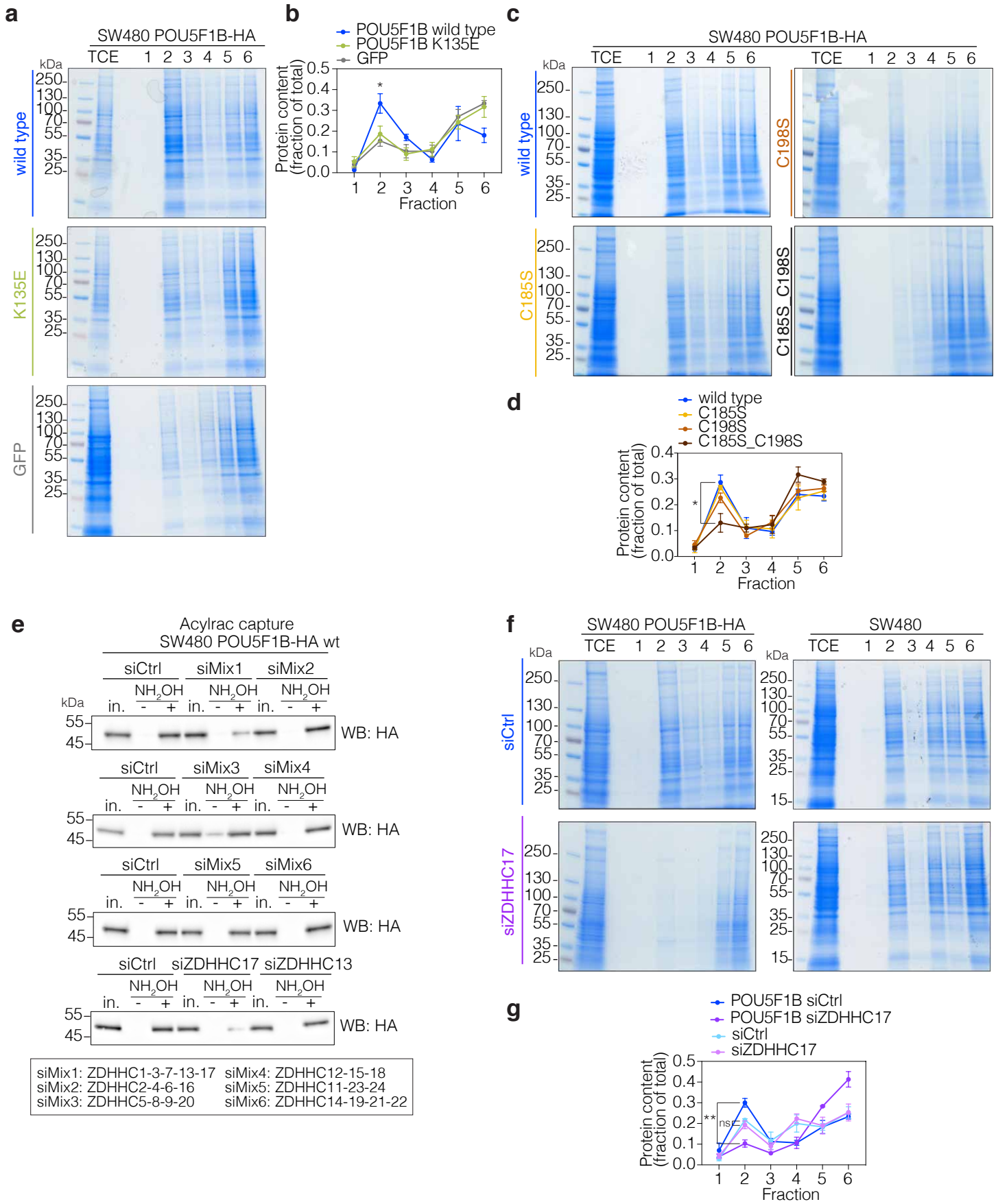

Supplementary Figure 2.ZDHHC17-mediated S-acylation is necessary for POU5F1B to increase the protein content of membrane nanodomains. a, Isolation of detergent-resistant membranes (DRMs) from POU5F1B-HA-wild-type-, -K135E-, and GFP-overexpressing SW480 cells, fractions were run on SDS-PAGE and gels were stained with Coomassie. 1-3 correspond to insoluble fractions, 4-6 to soluble fractions, DRMs being traditionally found in fraction 2. **b,** Quantification of coomassie staining in (a) (Fraction 2 wild type vs. K135E P=0.04; vs.GFP P=0.033 by t-test). **c,** Same as in (a) from POU5F1B-HA-wild-type-, -C185S-, -C198S-, and -C185S_C198S-overexpressing SW480 cells. **d,** Quantification of (c) (Fraction 2 in wild type vs. C185S P=0.561; vs.C198S P=0.163 ; C185S_C198S P=0.029 by t-test). **e,** Acylrac capture assay in siCtrl-, siRNA mix 1 to 6-, siZDHHC17-, and siZDHHC13-POU5F1B-HA SW480 cells. **f,** Same as in (a and c) from siCtrl- and siZDHHC17- POU5F1B-HA SW480 cells and SW480 wild type cells. **g,** Quantification of (f) (Fraction 2: POU5F1B siCtrl vs. POU5F1B siZDHHC17 P=0.002; siCtrl vs. siZDHHC17 P=ns by t-test). ns not significant, * pvalue<0.05, ** pvalue<0.01.

Supplementary Figure 3

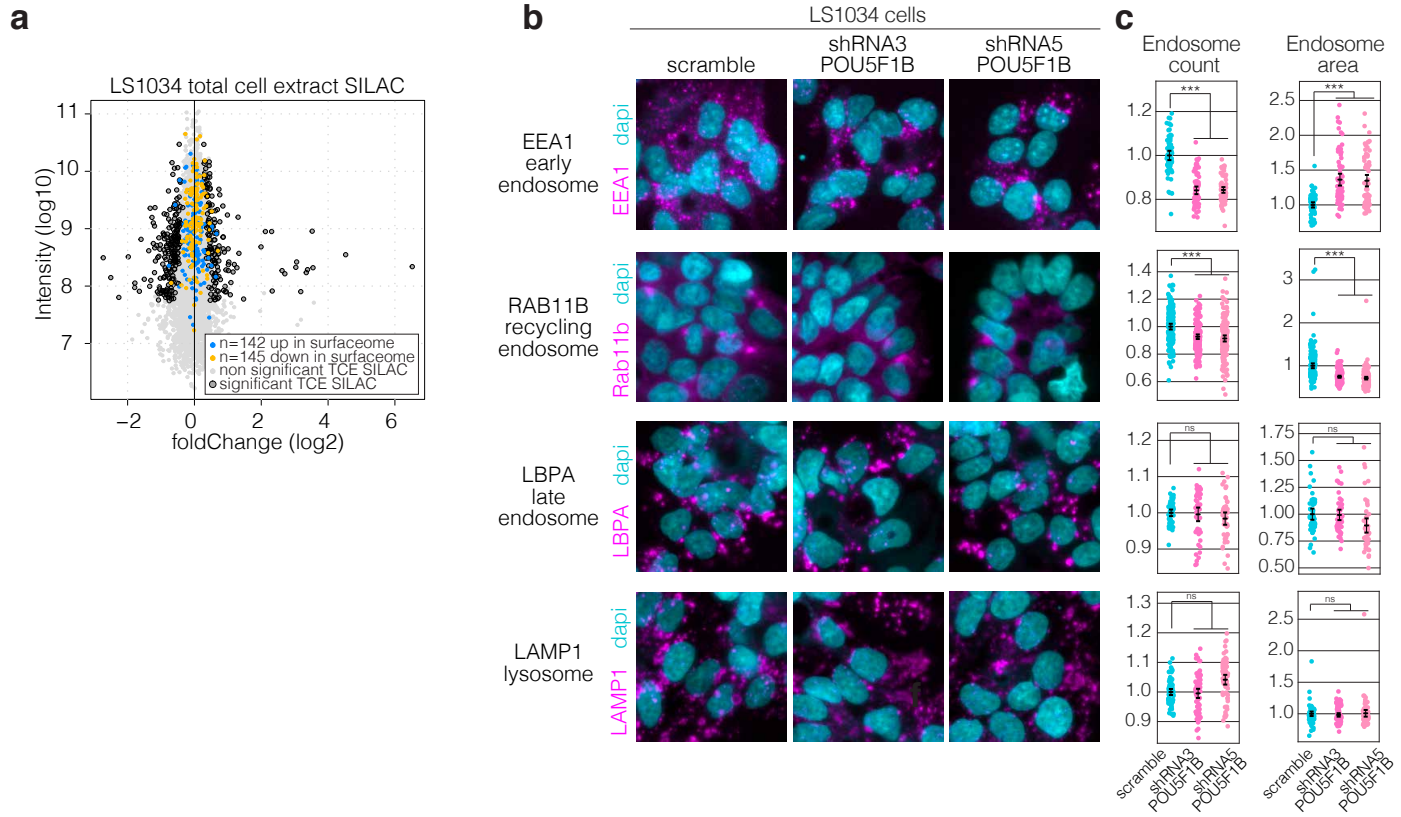

Supplementary Figure 3. POU5F1B triggers a redistribution of proteins towards the cell surface and stimulates the early-recycling endosomal pathway. a, MA plot depicting relative abundance and average intensity of individual proteins identified by SILAC in total cell extracts (TCE) of sh-scramble vs. shRNA3 & shRNA5 LS1034 cells (data from https://doi.org/10.1038/s41467-022-32649-7). Measurements were performed in independent duplicates, each dot represents a detected protein, with significantly changed ones ($P < 0.05$) circled in black. 142 upregulated and 145 downreguated proteins in the surfaceome from the same cells (Fig 3F) are colored in blue and yelow respectively. **b,** Representative immunofluorescence-confocal microscopy of sh-scramble, shRNA3, and shRNA5 LS1034 cells, with EEA1, RAB11B, LBPA, and LAMP1 lysosomes in magenta and the nuclear marker dapi in cyan. **c,** Endosome count and area quantification from cells in (b) (Respective count and area from EEA1 P=1.34e-33 P=3.27e-13; RAB11B P=6.94e-10 P=3.87e-25; LBPA P=0.29 P=0.11; LAMP1 P=0.06 P=0.82 positive endosomes in scramble vs. sh3&sh5 cells). ns, not significant, *** pvalue<0.001

Supplementary Figure 4

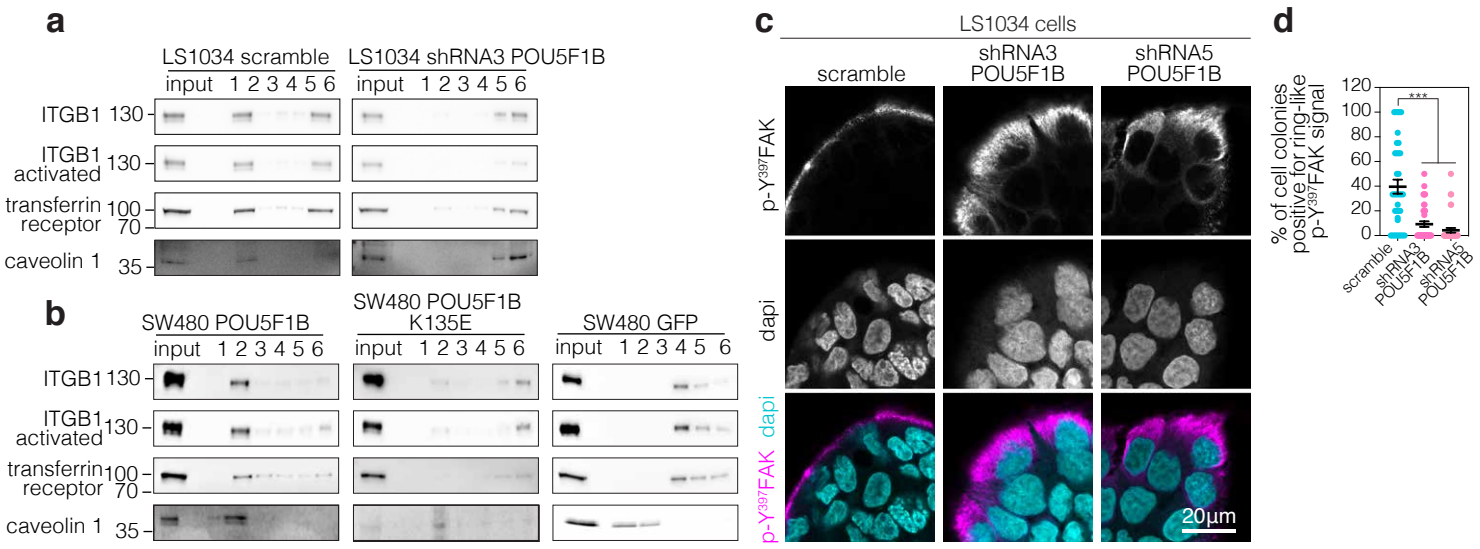

Supplementary Figure 4. POU5F1B induces accumulation of ITGB1 in DRMs and activated focal adhesion kinase (p-Y^{397} FAK) at the periphery of colorectal cancer cells. a, Western blot analysis of ITGB1 and activated ITGB1 in detergent-resistant membranes (DRMs) extraction from sh-scramble, shRNA3 & shRNA5 LS1034 cells, and **b,** POU5F1B-, POU5F1B-K135E- and GFP-overexpressing SW480 cells. Caveolin1 and transferrin receptor are used as controls for insoluble and soluble fractions, respectively. **c,** Representative immunofluorescence-confocal microscopy of cells presented in (a), with p-Y^{397} FAK in magenta and the nuclear marker dapi in cyan. **d,** Quantification of the percentage of cell colonies positive for peripheral ring-like p-Y^{397}FAK signal from cells in (c) (scramble vs. shRNA3 P=1.67e-05; vs. shRNA5 P=5.0e-08 by t-test). *** pvalue<0.001

Supplementary Figure 5

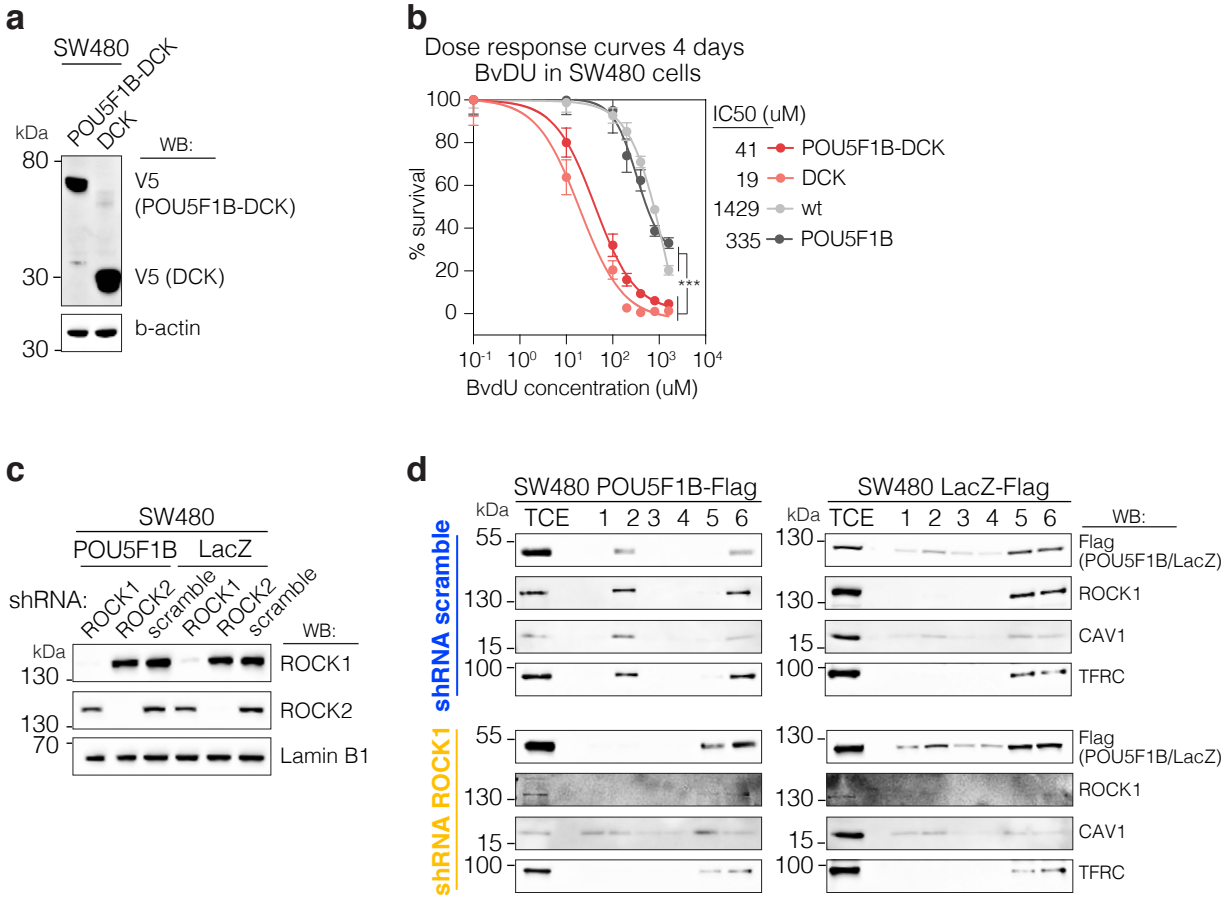

Supplementary Figure 5. Screening for inducers of POU5F1B degradation and examining their impact on DRMs. a, Immunoblot analysis of SW480 cells infected with the lentiviral vectors depicted in (Fig. 6A). **b,** 2-bromovinyldeoxyuridine (BvdU) dose response curves in wild type, DCK-, POU5F1B-DCK-, and POU5F1B-expressing SW480 cells, 4 days post-treatment (P = 9.7e-27 by extra sum-of-squares F-test). **c,** Immunoblot analysis of POU5F1B- and LacZ-expressing SW480 cells infected with lentiviral vectors expressing doxycycline-inducible shRNAs against ROCK1, ROCK2 and scramble sequences. **d,** Immunoblot analysis of ROCK1 and Flag-tagged POU5F1B and LacZ in detergent-resistant membranes (DRMs) extraction from sh-scramble and shROCK1 SW480 cells expressing either POU5F1B or LacZ. Caveolin1 and transferrin receptor are used as controls for insoluble and soluble fractions, respectively. *** pvalue<0.001.